TatA and TatB generate a hydrophobic mismatch that is important for function and assembly of the Tat translocon in *Escherichia coli*

Denise Mehner-Breitfeld[1], Michael T. Ringel[1], Daniel Alexander Tichy[1,2], Laura J. Endter[2], Kai Steffen Stroh[2], Heinrich Lünsdorf[3], Herre Jelger Risselada[2], and Thomas Brüser[1*]

[1]Institute of Microbiology, Leibniz Universität Hannover, Herrenhäuser Str. 2, 30419 Hannover, Germany; [2]Institute for Theoretical Physics, Georg August University Göttingen, Göttingen, Germany; [3]Helmholtz Centre of Infection Research, Inhoffenstraße 7, 38124, Braunschweig, Germany; [*] To whom correspondence should be addressed: Thomas Brüser, Institute of Microbiology, Leibniz Universität Hannover, Herrenhäuser Str. 2, 30419 Hannover, Germany; Tel. +49 511 762 5945; Fax: +49 511 762 5287; E-mail: brueser@ifmb.uni-hannover.de

Abstract

The Tat system translocates folded proteins across energy-transducing prokaryotic membranes. In the bacterial model system *Escherichia coli*, the three components TatA, TatB, and TatC assemble to functional translocons. TatA and TatB both possess an N-terminal transmembrane helix (TMH) that is followed by an amphipathic helix (APH). The TMHs of TatA and TatB generate a hydrophobic mismatch with only 12 consecutive hydrophobic residues that span the membrane. We shortened or extended this stretch of hydrophobic residues in either TatA, TatB, or both, and analyzed effects on transport functionality and translocon assembly. The wild type length functioned best but was not an absolute requirement, as some variation was tolerated. Length-variation in TatB clearly destabilized TatBC-containing complexes, indicating that the 12-residues-length is crucial for Tat component interactions and translocon assembly. Metal tagging transmission electron microscopy revealed the dimensions of TatA assemblies, which prompted molecular dynamics simulations. These showed that interacting TMHs of larger TatA assemblies can thin the membrane together with laterally aligned tilted APHs that generate a deep V-shaped groove. The conserved hydrophobic mismatch may thus be important for membrane destabilization during Tat transport, and the exact length of 12 hydrophobic residues could be a compromise between functionality and proton leakage minimization.

Introduction

Tat systems serve the purpose to transport folded proteins across energy-transducing membranes in bacteria, archaea, plastids, and some mitochondria (Cline, 2015; Hou & Brüser, 2011; Petrů et al., 2018). They minimally consist of two components, TatA and TatC (Jongbloed et al., 2004), but three-component TatABC systems are very common and found in the model Tat systems of *Escherichia coli* and plant plastids (Müller & Klösgen, 2005). TatA and TatB are structurally similar and evolutionary related (Yen et al., 2002). Both are membrane-anchored by a 13-15 residues long N-terminal transmembrane helix (TMH) that contains only 12 consecutive hydrophobic residues. This helix is connected to an amphipathic helix (APH) via a short hinge at the cytoplasmic surface of the membrane (Hu et al., 2010; Rodriguez et al., 2013; Zhang, Hu et al., 2014; Zhang, Wang et al., 2014, Figure 1A). The APH is followed by a negatively charged patch of residues in TatA (Warren et al., 2009), and more C-terminal regions are neither conserved nor functionally essential (Lee et al., 2002). TatC has six transmembrane domains with both termini on the cytoplasmic side (Behrendt et al., 2004; Rollauer et al., 2012). TatB interacts tightly with TatC, whereas TatA gradually dissociates during purifications (Behrendt et al., 2007; Behrendt & Brüser, 2014; Bolhuis et al., 2001). From studies employing cross-linking and fluorescent protein tagging, it is known that the TatA interaction with TatBC changes during the translocation cycle (Alcock et al., 2013; Cline & Mori, 2001; Mori & Cline, 2002; Rose et al., 2013). A subpopulation of TatA protomers interacts with TatBC in a way that is not affected by mutations in TatC that abolish substrate-binding (Behrendt & Brüser, 2014), and resting-state-contacts of TatA to TatC have been identified (Aldridge et al., 2014). It is clear that TatA assemblies undergo substrate-induced conformational changes that relate to Tat transport (Alcock et al., 2016; Aldridge et al., 2012; Hou et al., 2018), and that the TatABC components rearrange during the translocation cycle (Geise et al., 2019; Habersetzer et al., 2017).

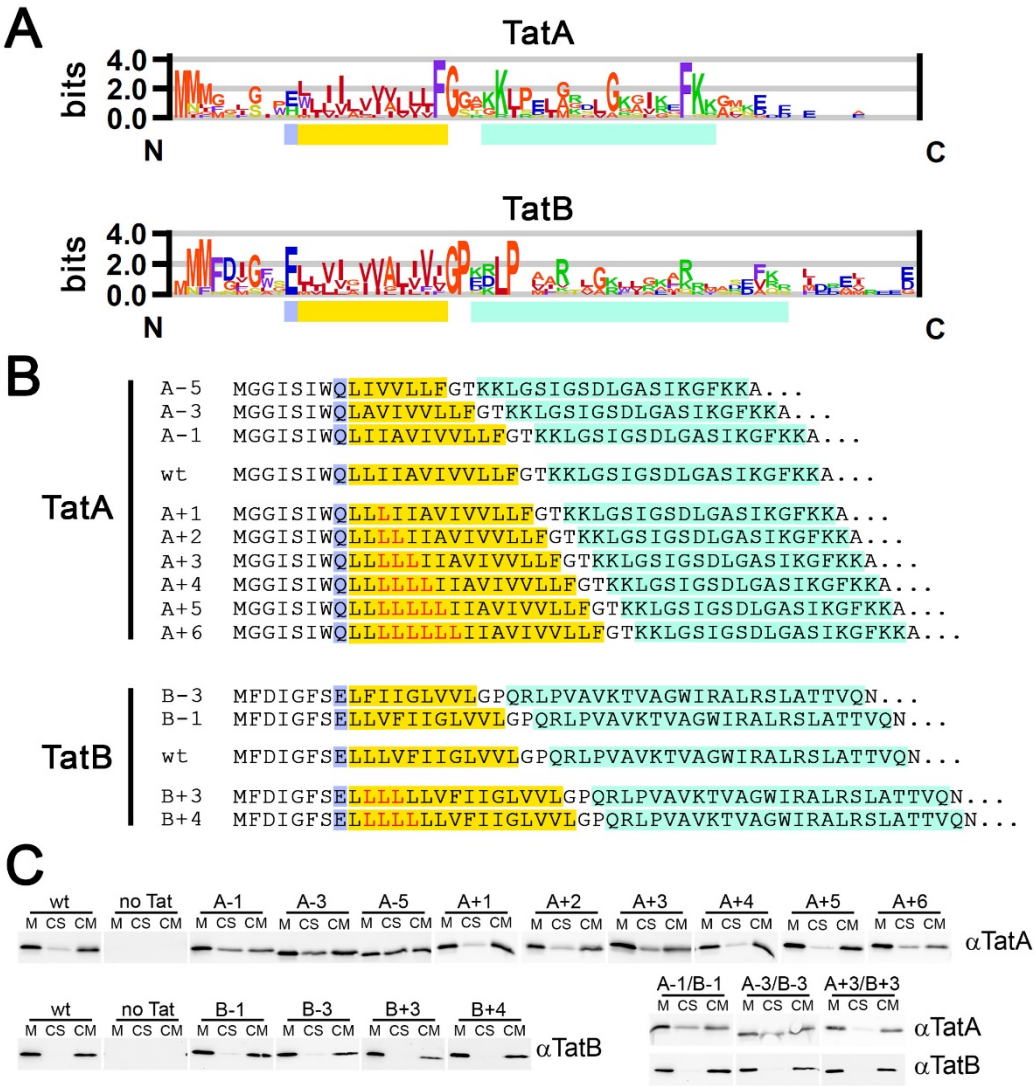

Figure 1: Constructs for the analysis of the 12-residues hydrophobic stretch in TatA and TatB. (A) Sequence logos of the functionally important region of TatA and TatB. Highlighted are the 12-residues hydrophobic stretch in the transmembrane helix of TatA and TatB (yellow), the preceding polar position (bluish purple), and the amphipathic helix (turquoise). The sequence logos have been obtained using enoLOGOS (Workman et al., 2005) based on sequence alignments by Clustal Omega (Sievers et al., 2011) of sequences from a wide range of organisms, including α-, β-, γ-, δ-, and ε-proteobacteria, firmicutes, actinobacteria, cyanobacteria, chlorobi, chloroflexaceae, thermodesulfobacteria, aquificae, and archaea. (B) TatA and TatB variants used in this study. The color code is the same as in (A). Inserted Leu residues are in red. (C) Carbonate wash analysis for the assessment of membrane integration of the TatA and TatB variants used in this study. TatA or TatB variants were detected by SDS-PAGE/Western blotting in the untreated membrane fraction (M), supernatant after carbonate wash (CS), and membranes after carbonate wash (CM). Note that all analyzed TatA and TatB variants are membrane inserted, but TatB variants are more stably membrane inserted than TatA variants, most likely due to their tighter interaction with TatC.

Tat-dependently transported proteins possess an N-terminal signal peptide that contains a highly conserved eponymous twin-arginine motif (Berks, 1996; Hou & Brüser, 2011). This motif is recognized by TatBC complexes that catalyze the membrane insertion of the signal peptide (Fröbel et al., 2012), whereas TatA is primarily required for the translocation step (Cline & Mori, 2001). TatA shows a high tendency to self-associate (Gohlke et al., 2005; Oates et al., 2005; Pettersson et al., 2021; Richter & Brüser, 2005), but high-resolution structures are only available for detergent-solubilized TatA (Hu et al., 2010; Rodriguez et al., 2013; Zhang, Hu et al., 2014), and the mode of TatA self-interactions in membranes is still unclear. Spin-labeling studies indicated that the transmembrane helices of TatA laterally interact (White et al., 2010), but only circular arrangements of aligned TatA have been suggested (Rodriguez et al., 2013), and the orientation of the APH has not been included in the latest models (Alcock et al., 2016). Interestingly, a dimeric structure of detergent-solubilized TatA indicated that also APHs of neighboring TatA protomers laterally interact (Zhang, Hu et al., 2014).

TMHs need to span the ca. 3 nm thick hydrocarbon core of membranes, and about 20 hydrophobic residues could in principle do this, but TMHs are in average 24.0 +/- 5.6 residues long (Baeza-Delgado et al., 2013), which is generally due to flexing or tilting of helices in membranes (Holt & Killian, 2010). It is therefore very unusual that TatA and TatB have membrane anchors with TMHs that contain only 12 consecutive hydrophobic residues. The exact length of this 12-residues stretch is strictly conserved from archaea to bacteria. It has been found that the TMH of TatA per se can destabilize membranes (Hou et al., 2018), but potential effects of helix shortenings or extensions have never been systematically analyzed. We therefore investigated effects of helix shortenings and extensions on Tat functionality and translocon assembly. Results indicate that both components tolerate smaller shortenings or extensions, but the natural 12 consecutive hydrophobic residues appear to function best. The hydrophobic mismatch is important for the stable interaction of TatB with TatC, and therefore the short helices most likely trigger also the association of TatA with TatBC. To find reasons for the conserved hydrophobic mismatch, we characterized TatA complexes by metal-tagging transmission electron microscopy (METTEM) and carried out MD simulations to analyze the behavior of TatA assemblies in membranes. As a result, we found that the short length of the TMH, together with the APH, permits a controlled local membrane thinning and destabilization, which likely is the basis for membrane permeabilization by Tat systems.

Results

Tat systems tolerate some shortening and extension of the stretch of 12 consecutive hydrophobic residues in the TMHs of TatA and TatB

To analyze the potential role of the short stretch of 12 consecutive hydrophobic residues in the TMHs of TatA and TatB, we shortened the hydrophobic helix by removing 1, 3, or 5 residues in TatA, and 1 or 3 residues in TatB. We also extended the helix by 1, 2, 3, 4, 5, or 6 leucine residues in TatA, and by 3 or 4 leucine residues in TatB (Figure 1B). In the following, the nomenclature of the constructs is facilitated for the reader, with "A+1" standing for the construct with one Leu inserted into the helix of TatA, and "B-3" standing for the construct with three hydrophobic residues deleted in the helix of TatB, as examples. To ensure the correct ratio of the Tat proteins, all genetic constructs were generated with the *tatABC* operon under control of its natural promoter in the Tat complementation vector pABS-*tatABC* (Berthelmann & Brüser, 2004). We used the *tat*-deletion strain DADE (Wexler et al., 2000) in combination with these vectors, which permitted functional analyses as well as BN-PAGE detections of the Tat complexes. All TatA and TatB variants were stably produced, and carbonate washes revealed that all of them were membrane-integrated (Figure 1C). A significant portion of all TatA variants was released from the membranes, which is already known for TatA and may be due to the presence of these proteins in destabilized membrane regions (Hou et al., 2018). The amount of TatA that was released by carbonate washes was higher in case of shortened TMHs (A-1, A-3, and A-5, Figure 1C). As TatA can destabilize membranes, these results may indicate that shorter membrane anchors enhance the membrane-destabilizing effect of TatA. TatB and its variants were more stable, which is expected as TatB tightly associates with TatC and should therefore be more stably membrane-integrated.

We analyzed Tat functionality with the described Tat systems. As Tat-deficient strains become SDS-sensitive, which relates to cell wall defects due to Tat-requirement for transport of the cell wall amidases AmiA and AmiC (Ize et al., 2003), we assessed Tat functionality by monitoring SDS resistance of the respective strains (Figure 2A).

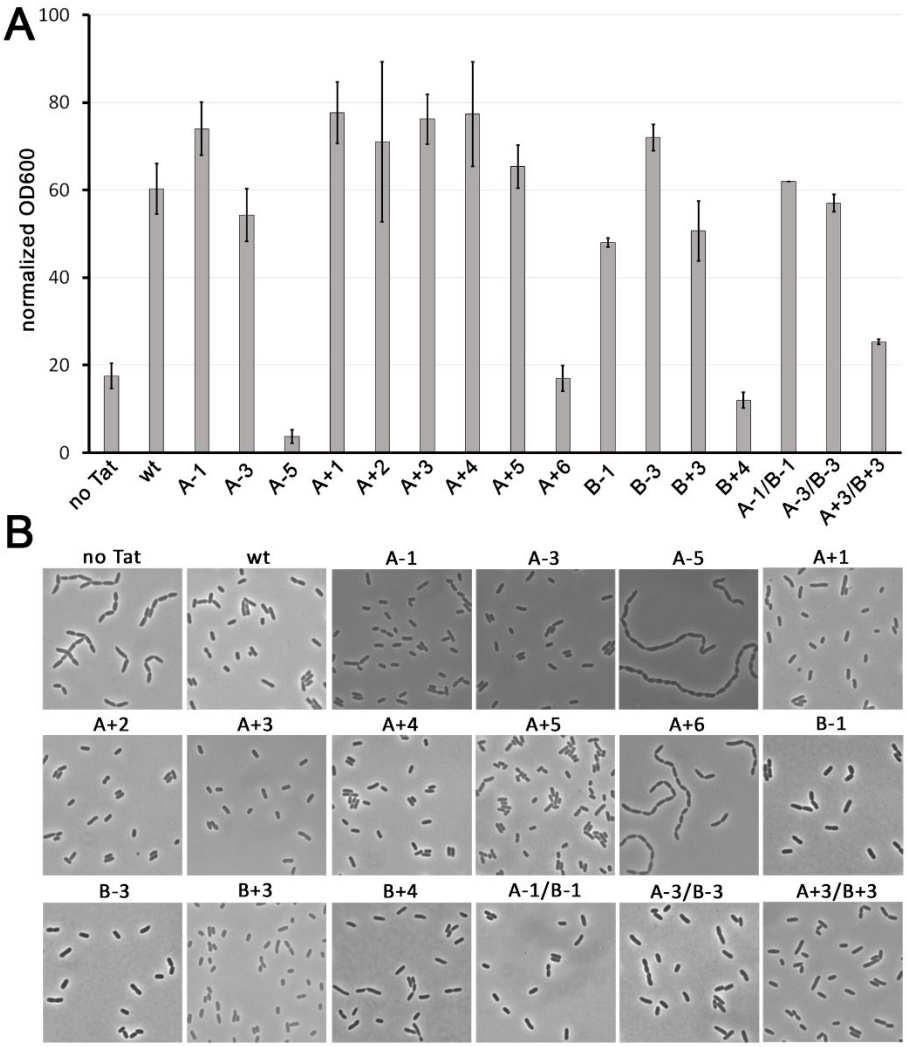

Figure 2: Physiological Tat functionality assays with mutated Tat systems. Complementation of SDS sensitivity (A) and chain formation (B) phenotypes of the Tat deficient strain DADE by Tat systems with indicated single or combined TatA and TatB variants. Controls: 'no Tat', empty vector control; 'wt', wild type Tat system.

Only the A-5 construct was inactive among the TatA variants with shortenings, and only the A+6 construct was inactive among the extension variants. The A-5 deletion variant showed higher sensitivity towards SDS then the non-complemented *tat* deletion strain, indicating that the A-5 variant was not only non-functional but also had an additional negative physiological effect.

In case of TatB, the B-1 and B-3 deletion-variants were both active in this assay, indicating that shorter hydrophobic helices in principle suffice to establish functional Tat translocons. This was unexpected as TatB tightly interacts with TatC for function, and we therefore expected less tolerance. The Tat system also tolerated the 3-residues extension in TatB, but not anymore the 4-residues extension. As TatA and TatB possibly could have overlapping functions and therefore could complement defects of each other, we also tested combinations of single and triple deletions in TatA and TatB, and triple extensions in TatA and TatB. Notably, the combined deletions were functional, indicating that indeed the deletions did not

115 inactivate the proteins. The combined extension (A+3/B+3) showed a markedly reduced SDS resistance,
116 indicating that some functional overlap had masked the effect of single +3 extensions. Nevertheless, the
117 partial SDS resistance proofed residual activity of A+3 and B+3 variants.
118 A second way to monitor functionality is the chain formation phenotype, which is similarly based on the
119 absence of AmiA and AmiC in the periplasm of Tat-deficient strains. If these amidases are not
120 transported into the periplasm, the murein is not efficiently hydrolyzed between separating cells, resulting
121 in chains of cells. In full agreement with the SDS-sensitivity measurements, the chain formation
122 phenotype was only observed in those strains that were also SDS-sensitive (Figure 2B). The strain with
123 the A+3/B+3 combination, which had reduced but not abolished SDS resistance, showed no chain
124 formation phenotype, indicating that sufficient amidases were transported for cell separation and
125 confirming the residual activity of the Tat system with the +3 extensions in TatA and TatB. In line with
126 that, the SDS-sensitive B+4 strain showed no obvious chain formation, indicating that transported
127 amidases sufficed for cell separation but not for SDS resistance.
128 To recognize weaker effects on protein transport, we then carried out biochemical analyses of the
129 transport of the Tat model substrate HiPIP, which is an iron-sulfur cluster containing protein that strictly
130 requires the Tat system for transport (Behrendt & Brüser, 2014). Subcellular fractions were prepared
131 from exponentially growing cells and analyzed by SDS-PAGE/Western blotting using antibodies
132 specifically recognizing HiPIP (Figure 3). We used a vector for low-level constitutive HiPIP production,
133 which results in complete translocation of HiPIP into the periplasm in case of fully functional Tat systems
134 (Brüser et al., 2003). In this assay, the mature periplasmic HiPIP band indicates transport, and any
135 precursor in the cytoplasm indicates reduced translocation relative to the fully functional Tat system. The
136 wild type Tat system, which served as positive control, showed a strong band of transported mature
137 HiPIP in the periplasm and no accumulation of precursor in the cytoplasm. Fractionation controls showed
138 that there was no leakage of cytoplasm into the periplasmic fraction, and the only faint mature HiPIP
139 band in the cytoplasm indicated little proteolytic cleavage of the signal peptide or residual periplasm in
140 the cytoplasmic fraction. The Tat deficient empty vector control strain did not show any transport and
141 instead the bands that are indicative for cytoplasmic accumulation of HiPIP, which are a strong
142 cytoplasmic precursor band and a band that is due to partial degradation of the signal peptide. All TatA
143 variants with shortenings showed detectable cytoplasmic precursor bands, with only very little precursor
144 accumulating in A-1 variants and larger quantities accumulating in A-3 variants. The A-5 variant was
145 inactive, with no detectable mature protein in the periplasm. The TatA variants with extensions showed
146 slightly less transport in the A+1 variant and only very little cytoplasmic precursor in the A+2, A+3, and

147 A+4 variants, but a sudden almost complete block of transport with the A+5 variant. The A+6 variant
148 was inactive. With the TatB variants, we observed little accumulation with the B-1 and B-3 variants,
149 indicating only a minor defect, whereas the B+3 variant strongly accumulated HiPIP in the cytoplasm
150 and the B+4 variant hardly transported HiPIP anymore. Interestingly, the combinations A-1/B-1,
151 A-3/B-3, and A+3/B+3 all showed a stronger effect than the single variants, indicating that the defects
152 were additive, or that there was indeed some partial compensation of defects of TatA by TatB or vice
153 versa detectable in this semi-quantitative assay. Such effects were more difficult to detect by the
154 apparently less sensitive amidase-based assays, in which few transported enzymes may often suffice for
155 physiological complementations (compare with the SDS sensitivity assay in Figure 2A).

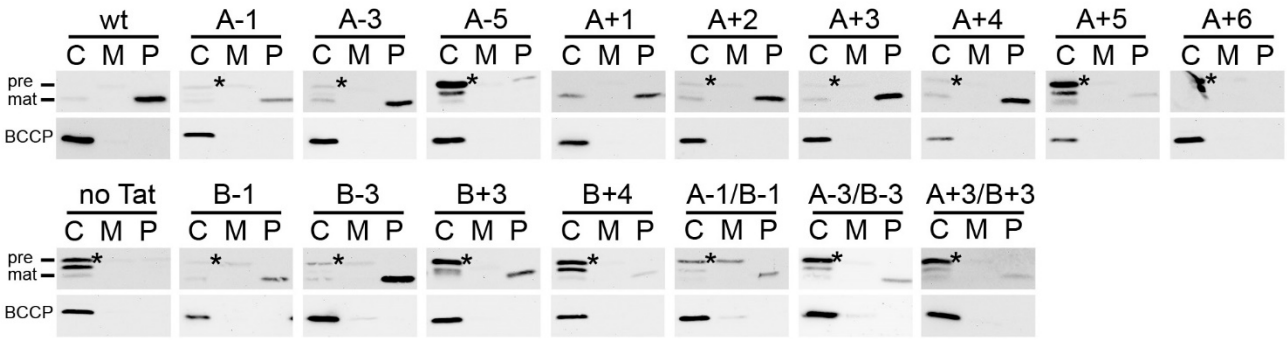

Figure 3: Biochemical Tat functionality assays with mutated Tat systems. Transport analysis by SDS-PAGE/Western blot detection of the precursor (pre, band at 14 kDa) and mature (mat, band at 11 kDa) forms of the Tat substrate HiPIP in subcellular fractions of cells containing the indicated single TatA or TatB variants or combinations thereof (upper blots). Biotin carboxyl carrier protein (BCCP, band at 22 kDa) was detected as fractionation control (lower blots). Cytoplasmically accumulating precursor is marked by asterisks. Note that any detection of mature protein in the periplasmic fraction indicates functional transport, whereas accumulation of precursor in the cytoplasm is only observed in cases of a partial or complete defect in transport. C, cytoplasm; M, membrane; P, periplasm.

156 Together, the activity measurements indicate that the 12-residues length of the hydrophobic helix in wild
157 type TatA and TatB results in highest transport efficiency. In case of TatA, shortenings by up to three
158 residues and extensions by up to four residues are tolerated, and some residual transport is even detectable
159 with a five-residues extension. TatB similarly tolerates shortenings and truncations of three residues,
160 with only little residual transport detectable in case of the four-residues extended B+4 variant.

Variation in the TatB TMH length, not in the TatA TMH length, interferes with TatBC complex stability

It is well-described that TatB interacts with the short helix 5 of TatC, whereas TatA can interact with the similarly short helix 6 of TatC (Alcock et al., 2016; Habersetzer et al., 2017). It was therefore possible that functional effects of length variations in the hydrophobic TMH of TatA or TatB are simply due to disturbed interactions with TatC. To examine this aspect, we analyzed the stability of the known TatC-containing complexes (Geise et al., 2019).

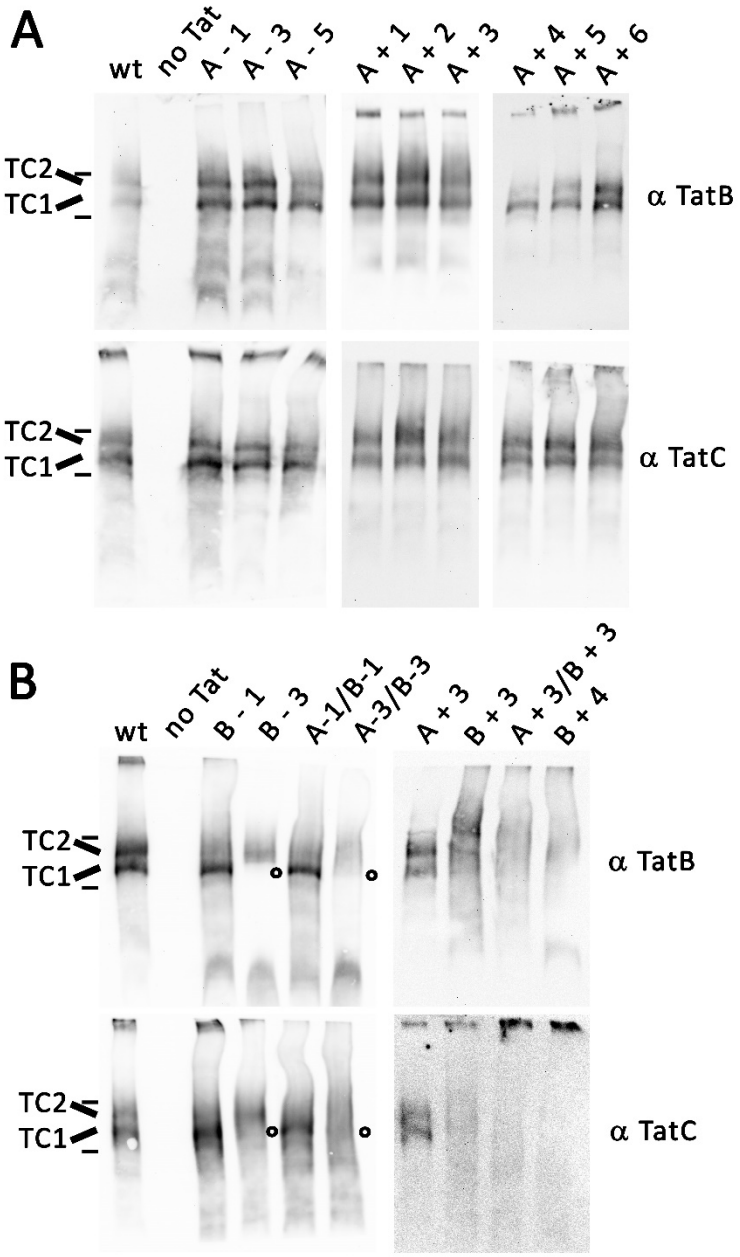

Figure 4: Analysis of Tat complexes in strains with mutated Tat systems. (A) BN-PAGE/Western blot detection of Tat complex 1 (TC1) and 2 (TC2) in strains containing Tat systems with indicated TatA variants (A) or with TatB variants alone or in combination with TatA variants (B). Blots were developed with antibodies against TatB (upper blots), or TatC (lower blots). The position without the TC1 band in B-3 Tat systems is highlighted by open circles. B+3 and B+4 extensions have more general destabilizing effects. For direct comparison, the A+3 system is analyzed in parallel with B+3 and the A+3/B+3 combination. Positions of TC1, TC2, and molecular weight markers (440 kDa, 669 kDa) are indicated on the left.

167 Membrane fractions were solubilized by digitonin and analyzed by BN-PAGE/Western blotting to detect
168 Tat complexes TC1 and TC2 (Figure 4). While the complexes were unaffected by the length variations
169 in TatA (Figure 4A), the B+3 and B+4 variants caused disassembly of the complexes (Figure 4B). In
170 case of B-1, only the TC2 band was affected and changed to a very diffuse band, whereas the TC1 band
171 remained unaffected. With B-3, the diffuse band of the size of TC2 was the only remaining complex, and
172 TC1 had completely disappeared. Some disassembly of Tat complexes is always observed and has been
173 described previously (Behrendt & Brüser, 2014). Together, these data clearly indicate a severe effect of
174 the TatB variants on TatBC interaction and consequently on TatBC complex stability. As also the
175 functional TatB variants showed this destabilizing effect, sufficient TatBC complexes must have been
176 present in living cells to support Tat transport with this expression system.

177 *METTEM-analysis of TatA clusters in the cytoplasmic membrane at wild type expression level*
178 If the specific length of the interacting TMHs would just be required for TatC interactions, such
179 interacting helices would not be expected to be extremely short. As TatA oligomers are present at TatBC
180 complexes during transport (Dabney-Smith et al., 2006), and as TatA contacts the mature domain of
181 substrates during transport (Pal et al., 2013; Taubert & Brüser, 2014), we attempted to characterize the
182 membrane-integral TatA associations in more detail, hoping to find clues for the functional role of the
183 short transmembrane helix. In earlier studies, fluorescence analyses of YFP-tagged TatA indicated that
184 in average 25 TatA protomers assemble in homooligomeric complexes (Leake et al., 2008). We intended
185 to see these complexes at higher resolution by METTEM, using the smaller metallothionein-gold tags
186 (Bouchet-Marquis et al., 2012; Diestra et al., 2009; Mercogliano & DeRosier, 2006, 2007; Morphew et
187 al., 2015; Nishino et al., 2007). In initial experiments with abundant recombinant Tat systems, we found
188 that three metallothioneins in row (= MT3) permitted clearly visible electron-dense granules of +/- 1 nm
189 in diameter in *E. coli* cells, and the detected particles could be identified as gold by PEELS analyses
190 (Figure 5).

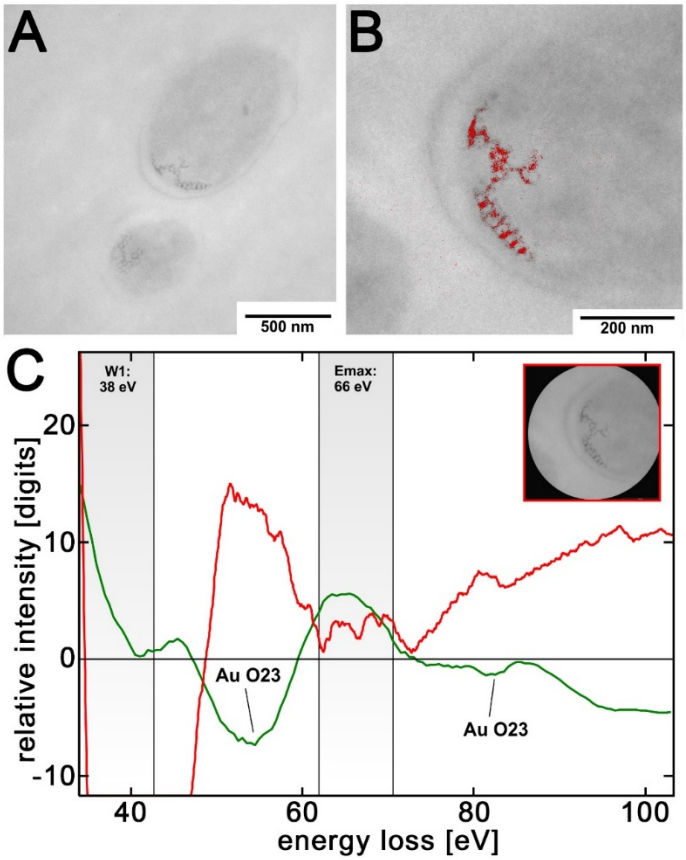

Figure 5: PEELS analysis of TatB-MT3-gold. (A) Survey micrograph of the analyzed cell containing the recombinant TatAB(MT3)C system as expressed by pABS-*tatAB(MT3)C*, with TatB-MT3-gold visible in clusters at the cell pole. (B) Electron spectroscopic element map at the Au-O23 edge Emax at 66 eV, energy-slit width: 8 eV, superimposed in red to the image of the cell pole shown in (A). Energy-settings and corresponding energy-slit width for the jump-ratio acquisition are indicated in C (W1; Emax). (C) PEEL-spectrum of the MT3-gold containing cell pole (inset: measuring area), detecting gold at the Au-O23 edge (red graph) and an energy maximum, which is in accordance to the Au-reference PEELS (green graph) from the EELS-atlas (Reimer et al., 1992).

Having the method established, we attempted to localize the Tat components at wild type expression levels in strains that had the modified *tat* operons chromosomally integrated. With TatB-MT3 and TatC-MT3, no gold was detectable at wild type level, but it was possible to detect TatA-MT3 in these experiments, which is likely due to the higher abundance of TatA relative to TatB and TatC in *E. coli*, which are present in an estimated 50:2:1 ratio, respectively (Jack et al., 2001). The wild type level of the TatA-MT3-abundance was confirmed by SDS-PAGE/Western blot analysis (Figure 6A). Substrates interact with the cytoplasmic face of TatA (Hou et al., 2018), and it is known that YFP tags (ca. 26 kDa) at the cytoplasmically located C-terminus of TatA inactivate TatA in the TatABC system of *E. coli* (Alcock et al., 2013). Similarly, we found that our MT3 tag (ca. 21 kDa) rendered TatA almost inactive (Figure 6B), as a slight activity was likely due to some degradation to mature size (Figure 6A). However, as only this tag permitted the direct visualization of TatA by TEM, we used it, keeping always in mind that the tag had sterically inactivated TatA.

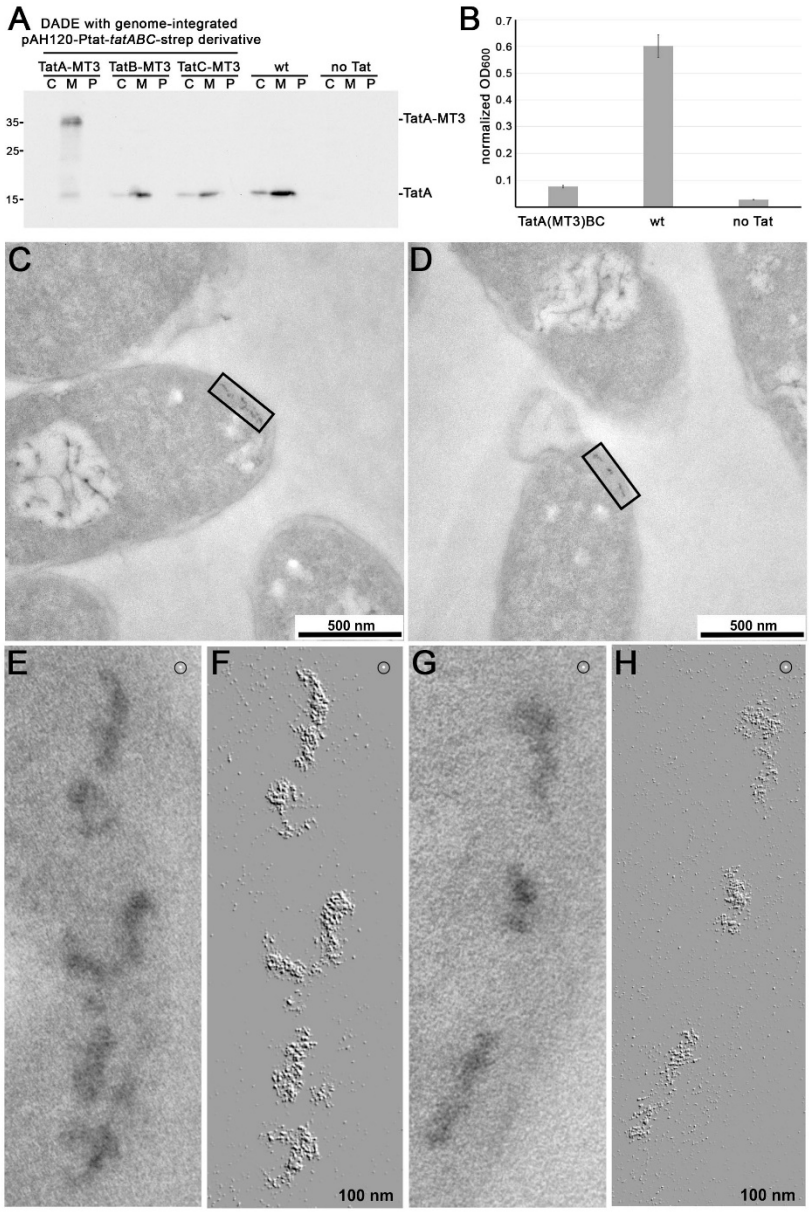

Figure 6: Detection of TatA-MT3-gold at wild type expression level. (A) Detection of TatA by SDS-PAGE/Western blot analysis in subcellular fractions of strains with MT3-tags at TatA, TatB, or TatC as encoded by single copy chromosomally integrated *tatABC-strep* operons. Wild type *E. coli* and the Tat-deficient strain DADE are analyzed for comparison. Positions of molecular weight markers are indicated on the left. C, cytoplasm; M, membrane; P, periplasm. (B) SDS-sensitivity measurements of strains with TatA(MT3)BC, TatABC (MC4100), or no (DADE) Tat system. (C) and (D) show overview images of cells with gold-labeled TatA-MT3-assemblies. Areas boxed in the respective overviews are shown below at higher magnification. (E) and (G) are original images, and (F) and (H) were topographically 'relief'-filtered to discriminate MT3-gold granules in pseudo-3D within TatA-MT3 assemblies. White 1 nm-dots (encircled in E,F,G,H) have been included as a direct scale for 1nm MT3-gold-granules.

TatA-MT3 formed gold assemblies near cell poles of irregular shape when seen in quasi top-view projection and roughly normal to the electron beam (Figure 6C-H). The mean length of the gold-assemblies was 20 nm ± 6.0 nm (N = 40, min = 10 nm, max = 37 nm). The width of the assemblies was about 10 nm. To determine the number of TatA-MT3 protomers in such assemblies, we counted the number of MT3-gold particles in 35 regions containing MT3-gold, and calculated from this the average number of 17 +/- 6 MT3-gold particles per 200 nm^2, which is the dimension of an average TatA-MT3-assembly. Interestingly, several of these assemblies visually appeared to be in contact, suggesting that they were somehow interdependent or connected (Figure 6E-H), which might be due to a clustering with

211 TatBC complexes. Sometimes, TatA-MT3-gold-assemblies appeared in longer linear arrangements in
212 the membrane. However, tilting of the sample revealed these arrangements to result from superposition
213 of individual assemblies when they are oriented in parallel to the electron beam within the ultrathin
214 section (Figure 7). In conclusion, TatA-MT3 formed longitudinal assemblies of irregular shape. The
215 number of subunits in such assemblies agreed with previous calculations that were based on fluorecence
216 microscopy (Leake et al., 2008).

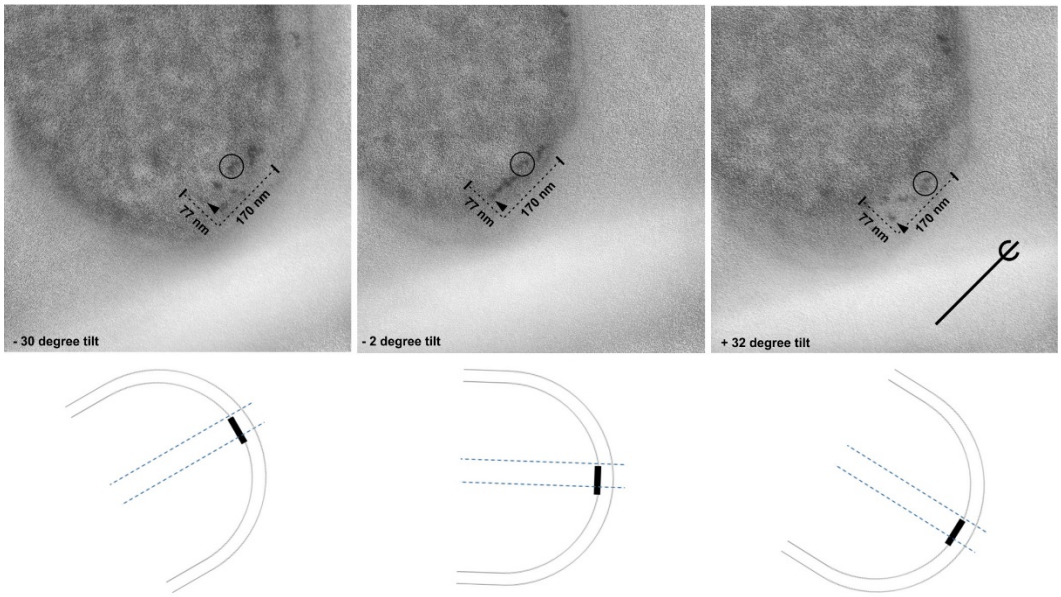

Figure 7: TEM-Tilting analysis of polar TatA assemblies. A seemingly very long TatA association, detectable by TEM of TatA-MT3-gold at a cell pole (middle), has been analyzed in the same cell by tilting the sample from -30° (left) to +32° (right). The tilted cell revealed that individual TatA-MT3 gold assemblies had been transformed into a single longer association due to superprojection of the assemblies when oriented parallel to the electron beam (tilt -2°).

217 *MD simulation indicates membrane thinning and lipid disorder generation by TatA clusters*

218 We then examined such linear TatA assemblies by 1500 nsec MD simulations with 22 TatA protomers
219 in the cytoplasmic membrane lipid bilayer, which is in the upper range of the observed TatA assemblies
220 and therefore might reflect functional associations at Tat translocons . The complex remained stable over
221 time, with the transmembrane helices in staggered rows (Figure 8A). Most APHs laterally contacted
222 neighboring APHs, with some interactions interrupted (Figure 8A), which agrees with the NMR evidence
223 for lateral APH helix association (Zhang, Hu et al., 2014), and these aligned APHs formed an angle of
224 in average 109° with the TMH, which agrees with solid state NMR analyses on *Bacillus subtilis* TatA
225 (Walther et al., 2010).

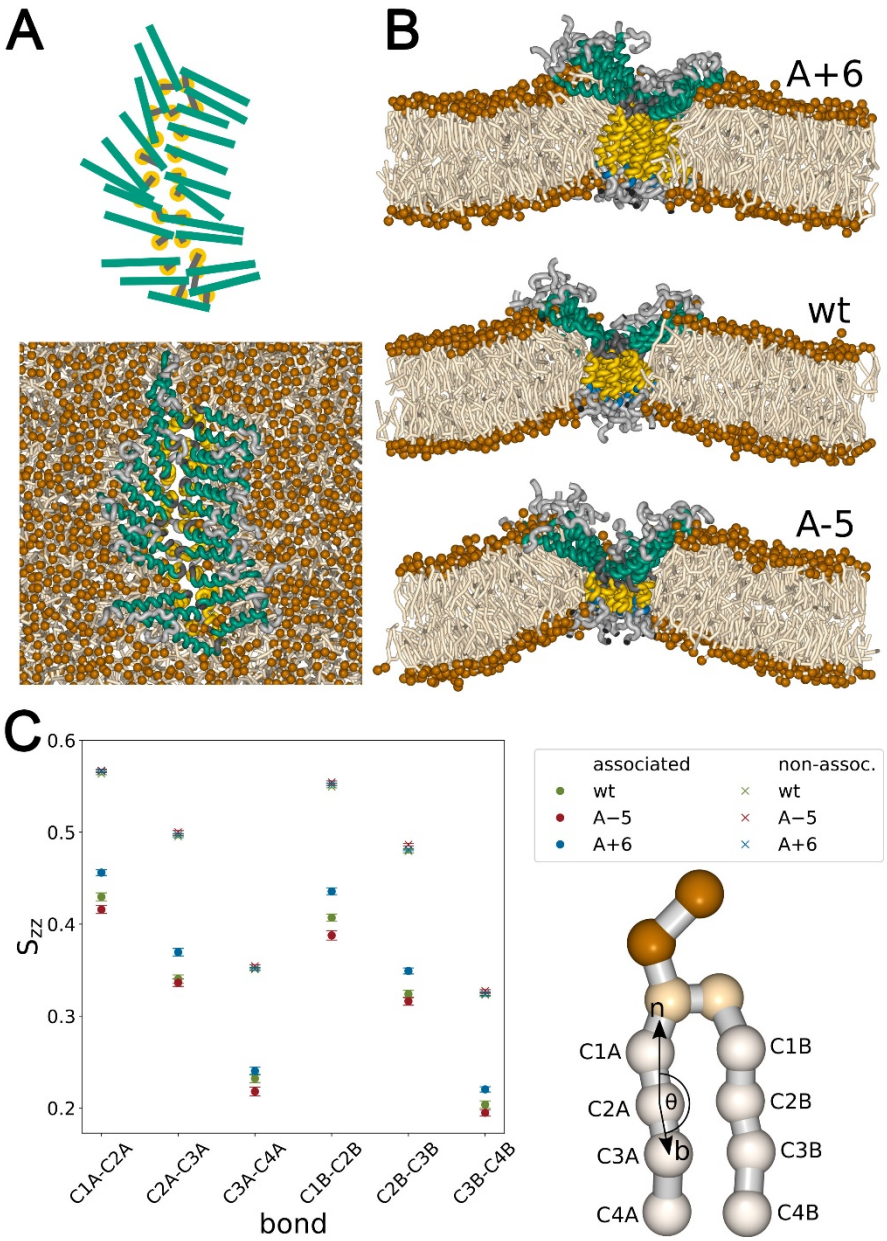

Figure 8: MD simulations with 22 TatA protomers of the wild type and the variants A-5 and A+6. (A) Top view from the cytoplasmic side on the 22 TatA wt simulation. (B) Cross sections through TatA complexes, with the cytoplasm above and the periplasm below the membrane cross sections. TMH, yellow; APH, cyan; Q8, turquoise; hinge region, dark grey; N- and C-termini, grey; lipids, light and dark (head groups) brown. (C) Lipid tail order parameter for lipids in the vicinity of the TMH (associated) and lipids in the bulk phase (non-associated). Bars indicate 95% confidence intervals. The shown coarse grained model of DPPE illustrates tail beads and the orientation of an example tail bond vector (b) relative to the bilayer normal (n), which is the basis for the order parameter. The other beads in the model are ethanolamine and phosphate (brown), and glycerol (light brown).

Also, the hinge was positioned deep in the membrane, which agrees with accessibility analysis data (Hou et al., 2018). The aligned APHs formed a deep V-shaped groove at the membrane surface (Figure 8B, see suppl. video 1). As a result of this constellation, the membrane was thinned to about half its natural thickness at the hinge region. A view on the lipids in this simulation revealed that the lipid head groups were excluded from areas of aligned APHs, and the acyl groups were therefore disordered and partly oriented in parallel to the APHs. The lipid disorder in the membranes could be quantified employing the lipid tail order parameter S_{zz} (Figure 8C). The data confirmed that the lipid order was lowered in the

environment of the APHs. We then carried out the simulations with the TatA variants A-5, A-3, A-1, A+1, A+2, A+4, and A+6. As now expected, the shortenings resulted in further thinning of the membrane, whereas the extensions of the TMH resulted in a thicker membrane, which becomes evident when comparing the simulations A-5, wt, and A+6 (Figure 8B). Accordingly, the lipid order further decreased with a shorter TMH and increased with a longer TMH (Figure 8C).

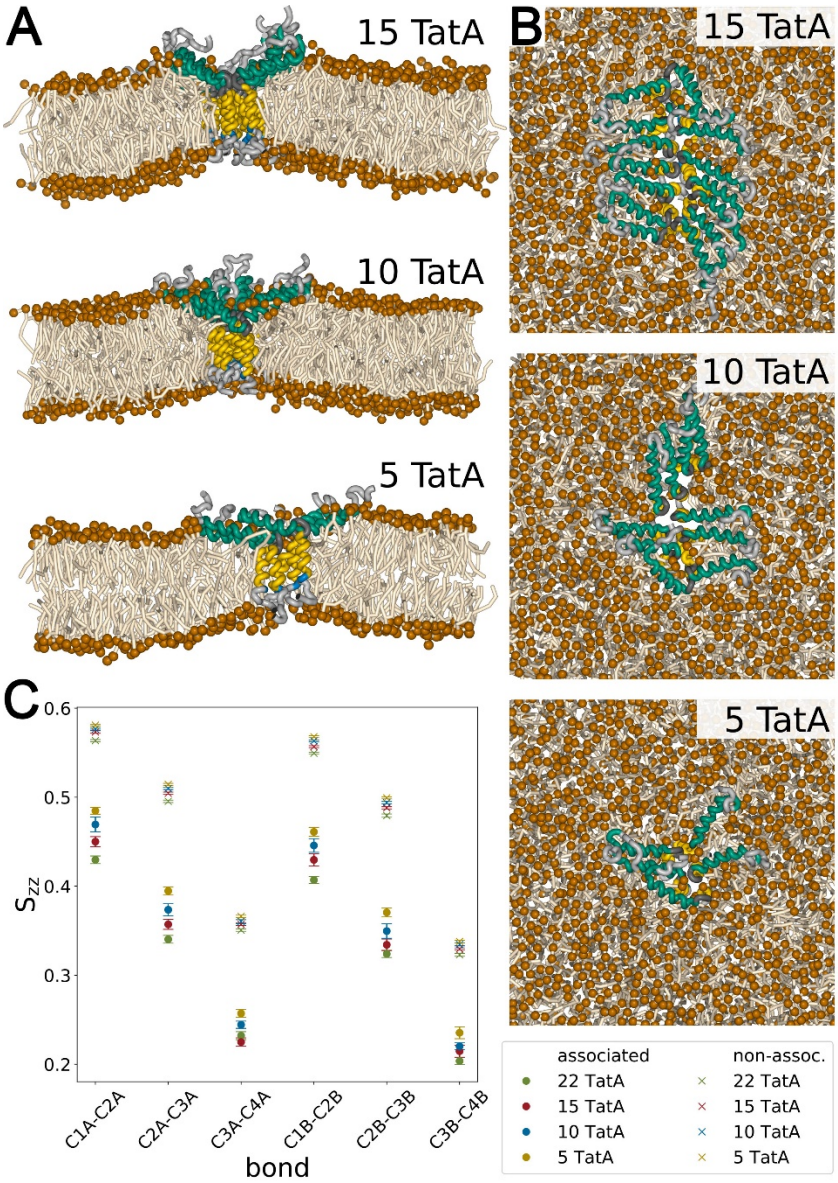

Figure 9: MD simulations with TatA complex of 15, 10, and 5 protomers. (A) Cross sections through TatA complexes. TMH, yellow; APH, turquoise; Q8, blue; hinge region, dark grey; N- and C-termini, grey; lipids, light and dark (head groups) brown. (B) Top views on the TatA complexes. (C) Lipid tail order parameter for lipids in the vicinity of the TMH (associated) and lipids in the bulk phase (non-associated). Bars indicate 95% confidence intervals.

Next, we addressed by MD-simulations whether the number of TatA protomers in the association could be relevant for membrane thinning. We repeated the simulations with 15, 10, and 5 TatA protomers, and found that the membrane-thinning effect required the lateral association of multiple APHs, which was the reason why only associations of >10 TatA protomers efficiently formed the V-shaped groove in the

242 membrane (Figure 9AB). In case of only 5 protomers, the lateral associations of APHs were too few to
243 impose a V-shaped groove on the membrane lipids, which is why such small associations had less effect
244 on the membrane bilayer, as quantified by the tail order parameter (Figure 9C, see suppl. video 2).

245 *Shortening of the TatA TMH can affect cellular growth*

246 The MD simulations shed some light on the mechanism, by which larger TatA assemblies can destabilize
247 the membrane. It has already been shown several years ago in *in vitro* experiments, that TatA can
248 destabilize the membrane and that substrate-binding to TatA enhances this membrane destabilization,
249 resulting in proton leakage (Hou et al., 2018). We thus wondered whether a too short or too long TMH
250 could result in extreme membrane destabilization *in vivo*, which could represent a selective pressure for
251 maintaining the exact length of 12 consecutive hydrophobic residues in TatA (and consequently also in
252 TatB and the short helices 5 and 6 in TatC, which need to assemble with TatA at the translocation site).

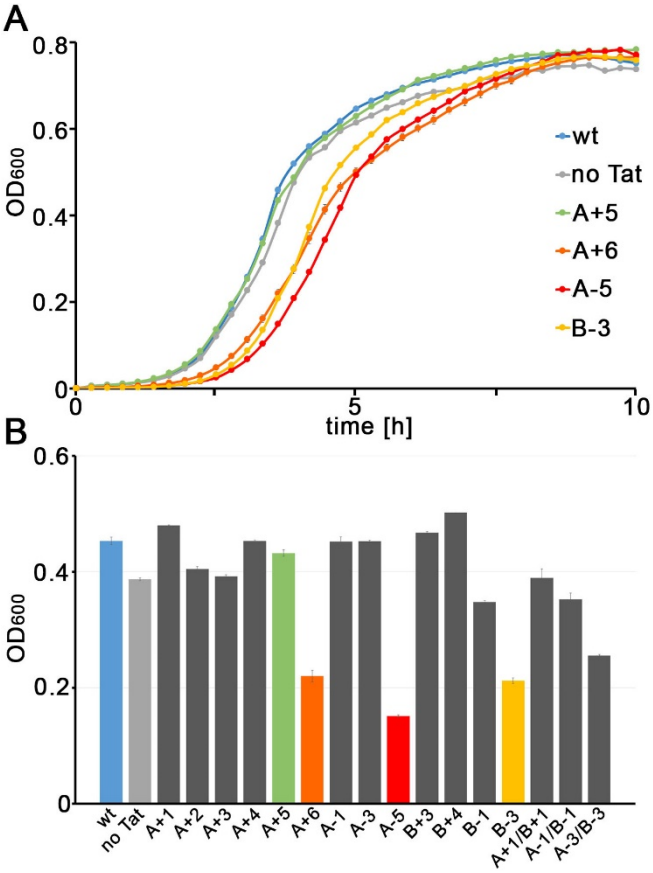

Figure 10: Growth analysis of strains containing the Tat systems analyzed in this study. (A) A-5, B-3, but also A+6 inhibit cellular growth. For comparison, strains with the wild type Tat system (wt) and without a Tat system (no Tat) are included, as well as the A+5 strain, which does not show a growth phenotype, although A+6 shows a clear growth phenotype. (B) Comparison of the growth phenotype of strains with all Tat systems used in this study, using the OD_{600} at the 3:36 h time point. For the strains shown in (A), the same color code is used. Error bars indicate the standard deviation of three cultures.

253 Growth curves indicated a delay of growth by A-5 and B-3, which may have been caused by cellular
254 adapations to stressed membranes (Figure 10). Interestingly, also A+6, not A+5, caused a clear growth

255 phenotype, which may be due to proton leakage as result of an influence on structures of other membrane
256 proteins.

257 Discussion

258 Helices that pass the bacterial cytoplasmic membrane have to traverse a hydrophobic environment of
259 about 3 nm (Katsuta et al., 2019). However, the TMH of TatA is predicted to consist of only 15 residues
260 (Zhang, Hu et al., 2014), and that of TatB consists of only 13 residues (Zhang, Wang et al., 2014), and
261 in these helices there is only a stretch of 12 consecutive hydrophobic residues. A helix of 12 residues has
262 a length of 1.8 nm, which does not suffice to span a lipid bilayer and therefore causes a hydrophobic
263 mismatch. Such mismatches often have functional implications, such as the regulation of the
264 mechanosensitive channel McsL or the aquaporin GlpF (Jensen & Mouritsen, 2004; Katsuta et al., 2019),
265 and hydrophobic mismatches can drive membrane protein interactions (Windisch et al., 2015). This study
266 now indicates that hydrophobic mismatches are also important for Tat functionality and Tat component
267 interactions. The length of 12 residues is not a strict requirement for Tat transport but rather an optimal
268 length, as little elongations and extensions of the TMH only reduce but not completely abolish function
269 and interactions (Figure 2 and 3). In case of TatB, our data show that all length variations affect TatBC
270 complex stability (Figure 4), and activity reductions are therefore likely due to weaker TatBC
271 interactions. It is interesting that specific variations of the TMH in TatB can have selective effects on the
272 different complexes, which might relate to conformational equilibria of the Tat complexes, such as
273 previously described for mutations in TatC (Geise et al., 2019). Observations of residual activity with
274 extended or shortened hydrophobic stretches in TatB are suggestive for significant flexibility of
275 interactions within TatBC complexes, which likely are not rigid but rather dynamic oligomers. Also in
276 case of TatA, a compromised interaction with TatB and/or TatC could contribute to the observed
277 transport defects. The TatA TMH can occupy the same TatC binding site as TatB (Habersetzer et al.,
278 2017), and as this TatC interaction is important, length variation in the TMH of TatA is expected to
279 influence activity of the system, as does the length variation in the TMH of TatB.
280 However, the task for Tat systems is the transport of folded proteins across membranes, and the strict
281 conservation of this short length of the membrane-spanning helix cannot be simply explained by TatC
282 interactions. If only the TatC interaction would be important, one would expect usual helix lengths for
283 the interacting helices and significant variation of the helix lengths among Tat systems from evolutionary
284 distant organisms. As this is not the case (Figure 1A), the extremely short TMHs of TatA and TatB thus
285 seem to have a specific reason that is much more restrictive that just the mediation of an interaction. Our
286 data indicate that the generated hydrophobic mismatch could be a delicate compromise between transport

287 efficiency and proton leakage. The hydrophobic mismatch TatC helices 5 and 6 in conjunction with the
288 TMH of TatB will attract TatA oligomers to the TatBC complex. It is possible that conformational
289 transitions upon substrate-binding enhance this hydrophobic mismatch at TatBC complexes and thereby
290 trigger this association, which has been observed with XFP-fusion proteins (Alcock et al., 2013; Rose et
291 al., 2013). We detected highly variable assemblies of in average 17 TatA protomers, and these assemblies
292 usually clustered in polar regions of the cells, suggesting some kind of interaction that may have been
293 mediated by the other Tat components (Figure 6). The number of TatAs in these assemblies was in good
294 agreement with published calculations that are based on YFP fusions (Leake et al., 2008).
295 Our data are in accord with the membrane-weakening and pulling model for the Tat mechanism (Brüser
296 & Sanders, 2003). An NMR study of the TatA structure already noticed this hydrophobic mismatch and
297 suggested that the polar end of the TMH deeply reaches into the bilayer, which could cause a thinning of
298 the membrane in case of assemblies with multiple TatA protomers (Rodriguez et al., 2013). However,
299 our MD simulations suggest that in a resting state it is the hinge region that resides deep in the membrane,
300 and that the lateral association of multiple tilted APHs generates a V-shaped groove in the membrane
301 (Figure 8). Membrane weakening by the TMH of TatA has been experimentally demonstrated *in vivo*
302 and *in vitro*, and it has been shown that the APH of TatA counterbalances this membrane weakening in
303 a resting state (Hou et al., 2018), which can be explained by the simulated structures. Importantly,
304 substrate interaction with TatA has been shown to trigger membrane permeabilization *in vitro*, which
305 thus could be a step of the translocation pathway (Hou et al., 2018). In fluorescence quencher
306 accessibility assays, the hinge region was not accessible in the resting state and became accessible in a
307 substrate-interacting state (Hou et al., 2018). The APH thus changes its orientation upon substrate-
308 association, exposing its N-terminal region to solvent, which enhances membrane destabilization and
309 therefore could be a trigger for transport (Hou et al., 2018). If the TMHs would be shorter than 12
310 residues, they might destabilize the membranes to an extent that would allow continuous uncontrolled
311 proton leakage, which would be a high energetic burden for the cells. Our growth experiments are already
312 supporting this hypothesis, as they demonstrate a growth effect of A-5 and B-3, and effects of minor
313 changes in TMH length on the cellular energetization may be similar but too small to be readily detectable
314 under the experimental conditions. The MD-simulated TatA assemblies visualize this aspect by showing
315 the extreme effect of TMH shortenings on membrane thickness. The lipid tail order parameter clearly
316 indicates a correlation of TMH length and membrane destabilization (Figure 8C). Also important is the
317 finding that a larger association of TatAs is required for an efficient membrane destabilization, and that
318 the generation of the V-shaped groove comes along with generation of membrane curvature (Figure 9).

The simulations fully agree with published data: The APHs laterally interact, as previously evidenced by NMR (Zhang, Hu et al., 2014), the TMHs laterally interact, as suggested by previous spin-labeling EPR studies (White et al., 2010), the hinge domain is deep inside the membrane, as seen in fluorescence quencher accessibility studies (Hou et al., 2018), and the APHs have a tilted orientation in the membrane, as seen in solid state NMR studies with *Bacillus subtilis* TatA (Walther et al., 2010). It is noteworthy that the average angle of the APH relative to the TMH in the simulations was near 109°, which is in good agreement with the angle determined by solid state NMR (Walther et al., 2010). The transmembrane helices are on a staggered position interacting with each other, sometimes with irregularities that form kinks in the linear assemblies. The MD simulation certainly could not include any information about interactions with TatBC complexes, whose structure is not known yet, but the TatC monomer structure is known and the interaction sites with TatB at helix 5 and TatA at helix 6 (Habersetzer et al., 2017; Rollauer et al., 2012). When combining this information with our MD simulations, it is now obvious that a linear TatA assembly could dock at this site (see Figure 11). In principle, such an interaction would explain why most TatA is lost during purification of TatBC complexes, and this model also explains how a simple conformational shift of TatC helices 5 and 6 in response to substrate binding may enhance the hydrophobic mismatch at the TatBC core to induce the binding of a large number of TatA protomers to the translocation site, which induces membrane destabilization where it is needed (Figure 11).

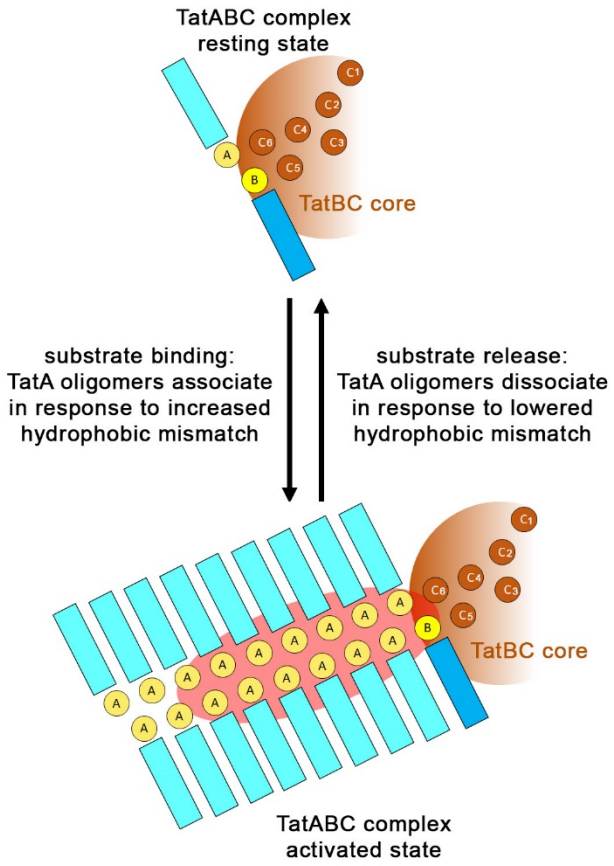

Figure 11: Potential substrate-induced assembly of membrane-weakening TatA-clusters at TatBC core complexes. Top view on the cytoplasmic face of the membrane, only positions of TMHs and APHs are schematically indicated. TMHs of TatA, TatB, and TatC are labeled A, B, or C, respectively. In case of TatC, which has 6 TMHs, the helix number is also indicated. The destabilized membrane region is highlighted by a reddish background. Only one docking site for TatA at the oligomeric TatBC core complex is exemplified in the scheme. The substrate that induces the conformational switch is only mentioned but not shown for clarity reasons. The color code for the TMHs and APHs is taken from Figure 1. See text for details.

338 The model also gives an idea about the region of membrane destabilization, which is essentially the
339 region underneath the APHs. There are two plausible pathways through the destabilized membrane: (1)
340 The two staggered rows of TatA, which are vis-à-vis positioned in the cluster, could open and permit the
341 passage of the Tat substrate, or (2) the TMHs remain in the center of the association and the substrate
342 passes through the thinnest point of the destabilized membrane close to the center of the TatA cluster.
343 As Tat substrates can be large in diameter, it is likely that both happens: TMHs will lose their contact
344 and APHs likely will dissociate to permit the passage of globular proteins. In such a situation of disorder,
345 it could well be that TatA exchanges with TatB at its TatC binding site, especially when the system is
346 saturated with transported substrates (Habersetzer et al., 2017). It is also possible, that an opening of
347 TatBC complexes can contribute to the TatA recruitment, such as proposed previously (Alcock et al.,
348 2016). Our simulations show that TatA forms linear clusters with two interacting rows of TMHs in the
349 center. From the energetic point of view, MD simulations indicate that there will not be any stable ring
350 shaped TatA assembly with an aqueous hole (Rodriguez et al., 2013), and that the hydrophobic mismatch
351 triggers linear associations of the TMHs (Figures 8, 9), but during the passage, transient aqueous holes
352 would be formed that would cause uncontrolled proton flux for a very short time-span. Such a proton
353 leakage would agree with the finding that about 80,000 protons pass through the membrane per
354 transported protein (Alder & Theg, 2003), albeit proton flux does not energize the transport (Bageshwar
355 & Musser, 2007; Braun et al., 2007). Although it is clear from these studies that the electric potential is
356 required at certain steps of the pathway, one of which may well be the proposed conformational transition
357 of the TatBC core complex that induces the recruitment of TatA (which is PMF-dependent; Alcock et
358 al., 2013; Rose et al., 2013), the driving force for the transport remains to be clarified. In principle, it
359 would be possible that the transmembrane signal peptide insertion as catalyzed by TatBC complexes
360 (Fröbel et al., 2012) constitutes this driving force, as the signal peptide remains bound to the TatBC
361 complex during transport of the mature domain (Gerard & Cline, 2006). Future experiments surely will
362 shed further light on this highly fascinating transport system.

363 Materials and Methods

364 *Bacterial strains and growth conditions* - The *E. coli ΔtatABCD ΔtatE* strain DADE (Wexler et al.,
365 2000), which is a derivative of the strain MC4100 (Casadaban, 1976), was used for localization and
366 complementation studies. *E. coli* XL1-Blue Mrf' Kan (Stratagene, La Jolla, California, USA) or *E. coli*
367 DH5α λ *pir*$^{+}$ were used for cloning. Unless otherwise stated, bacteria were grown aerobically at 37°C on
368 LB medium (1% (w/v) tryptone, 1% (w/v) NaCl, 0.5% (w/v) yeast extract) in the presence of the
369 appropriate antibiotics (25 µg/ml chloramphenicol, 100 µg/ml ampicillin, 12.5 µg/ml tetracycline, 15

370 µg/ml kanamycin). For subcellular fractionations, all cultures were normalized to an OD_{600} of 1.0. For
371 growth curves, the OD_{600} was measured in 15-min intervals with cultures grown at 37°C in shaking 96-
372 well plates (culture volume: 200 µl), using the SpectraMax iD3 Microplate Reader (Molecular Devices,
373 LLC., San José, California, USA).

374 *Genetic Methods and Plasmids* - For analyses of Tat functionality and for optimization of the MT3-gold-
375 labeling method, the TatABC components were constitutively overproduced using the natural P_{tatA}
376 promoter and *tatABC* operon organization in plasmid pABS-*tatABC* and derivatives thereof
377 (Berthelmann & Brüser, 2004). The shortenings and extensions of the hydrophobic helices in TatA and
378 TatB were carried out by QuikChange mutagenesis. Primers are listed in Table 1.

Table 1: Primers used in this study[1].

Mutagenesis Primers[2,3]	Sequence (5'>3')
Deletions	
tatA-1-F	CAGTATTTGGCAGTTAATTATTGCCGTCATCG
tatA-3-F	GTATTTGGCAGTTAGCCGTCATCGTTG
tatA-5-F	GGTATCAGTATTTGGCAGTTAATCGTTGTACTGCTTTTTGGC
tatB-1-F	CGGTTTTAGCGAACTGTTGGTGTTCATCATC
tatB-3-F	GTTTTAGCGAACTGTTCATCATCGGCC
Leucine insertions	
tatA+1-F	CAGTATTTGGCAGTTATTGCTTATTATTGCCGTCATCGTTG
tatA+2-F	CAGTATTTGGCAGTTATTGCTTCTCATTATTGCCGTCATCGTTG
tatA+3-F	GGCAGTTATTGCTTCTCTTAATTATTGCCGTCATCG
tatA+4-F	GGCAGTTATTGCTTCTCTTATTGATTATTGCCGTCATCG
tatA+5-F	GTTATTGCTTCTCTTATTGCTTATTATTGCCGTCATCGTTG
tatA+6-F	GTTATTGCTTCTCTTATTGCTTCTCATTATTGCCGTCATCGTTG
tatB+3-F	CGGTTTTAGCGAACTGCTGCTCCTTCTATTGGTGTTCATCATC
tatB+4-F	CGGTTTTAGCGAACTGCTGCTCCTTCTGCTATTGGTGTTCATCATC
Fusion Primers	
MT-I-F	CGACCGGGATCCAATTCGAGCTCGAACAACAACAAC
MT-R	TTATCGGCGCGCTTGTAAAACGACGGCCAGTGC
pABS-*tatB*-BamHI-F	CCCGAGGGATCCGATAAAGAGCAGGTGTAATCC
pABS-*tatC*-ClaI-R	GGCCGTATCGATCTATTCTTCAGTTTTTTCGCTTTCTGCTTC
pABS-*tatA*-MT3-R	GTTGTTGTTGTTCGAGCTCGAATTAGATCCCACCTGCTCTTTATCGTGGCGCTTCG
pABS-*tatABC*-SalI-F	AGGGCATCGGTCGACGCTCTCC
pABS-*tatB*-MT3	GTTGTTGTTGTTCGAGCTCGAATTAGATCCCGGTTTATCACTCGACGAAGGGGAAG
pABS-*tatC*-F	CCGAGCGGATCCTCGTCGAGTGATAAACCGTAAAC
Primers for cloning of pAH120-Ptat-*tatABC*-strep	
tatA-NdeI-F	GAACACATATGGGTGGTATCAGTATTTGGC
tatC-BamHI-R	AAGGATCCTTCTTCAGTTTTTTCGCTTTCTGC

[1]*Primer sequences are given in 5'-3' direction.* [2]*Corresponding reverse primers covered the same sequence.*
[3]*Templates for larger deletions or insertions were the constructs with smaller deletions or insertions.*

379 To analyze MT3-gold labeled Tat components at wild type level, the *tatABC* operon and its derivatives
380 were cloned into pAH120-Ptat-*tatABC*-strep (see primer table), which is a *tatABC*-containing derivative
381 of pAH120-Ptat-*tatA*-strep-ΔBamHI (Taubert et al., 2015). Briefly, the MT3-tag (including the linker)
382 was amplified from the pMAL-c2x-MT3 (Diestra et al., 2009) using primers MT-l-F and MT-R, cut with
383 BglII/BssHII, and ligated into the backbone of the plasmid pAH120-Ptat-*tatABC*-strep cut with
384 BamHI/BssHII. This resulted in pAH120-Ptat-*tatABC*-MT3, which was then cut with NdeI/BamHI and
385 ligated into the corresponding sites of pABS-*tatABC*-H6 (Geise et al., 2019), resulting in pABS-*tatABC*-
386 MT3. To construct pABS-*tatA*-MT3, *tatA* was amplified from pABS-*tatABC*-MT3 using primers pABS-
387 *tatA*-MT3-R and pABS-*tatABC*-SalI-F, the fragment was cut with SalI/SacI and ligated into the plasmid
388 backbone obtained by restriction of pABS-*tatABC*-H6 with the same enzymes. The same procedure was
389 followed to construct pABS-*tatAB*-MT3, except that the primers utilized were pABS-*tatB*-MT3-R and
390 pABS-*tatABC*-SalI-F. To append the *tatBC*-genes to the *tatA*-MT3-construct, these were amplified from
391 the pABS-Ptat-*tatABC*-MT3 plasmid using primers pABS-*tatB*-BamHI-F and pABS-*tatC*-ClaI-R, the
392 fragment was cut with BamHI/ClaI and ligated into the respective sites of the pABS-Ptat-*tatA*-MT3
393 backbone. The same steps were taken to construct the pABS-*tatAB*-MT3-*tatC* plasmid, only that primers
394 pABS-*tatC*-F and pABS-*tatC*-ClaI-R were used and the fragment was ligated into the backbone of
395 pABS-Ptat-*tatAB*-MT3. Finally, both the *tatA*-MT3-BC and *tatAB*-MT3-*tatC* constructs were transferred
396 back into pAH120 by restriction of pAH120-Ptat-*tatABC*-MT3, pABS-*tatA*-MT3-*tatBC* and pABS-
397 *tatAB*-MT3-*tatC* with NdeI/XbaI, and ligation of the *tat*-fragments into the pAH120-backbone. Vectors
398 were integrated into the chromosomal lambda attachment site according to the protocol of Haldiman and
399 Wanner (Haldimann & Wanner, 2001). pRK-*hip* was used for constitutive low-level expression of the
400 *hip* gene from its own promotor (Brüser et al., 2003).
401 *Biochemical methods* - Subcellular fractionations into periplasm, membranes, and cytoplasm were
402 performed with 50 mL cultures as described previously (Taubert et al., 2015). SDS-PAGE analysis was
403 carried out by standard methods (Laemmli, 1970). BN-PAGE was performed as described previously
404 (Richter & Brüser, 2005), but without *β*-mercaptoethanol in the buffers. TatABC complexes were
405 solubilized with 1% digitonin. For immunoblots, proteins were semi-dry blotted on nitrocellulose
406 membranes and blots were developed using antibodies directed against synthetic C-terminal peptides of
407 TatA, TatB, TatC or polyclonal rabbit serum against purified HiPIP, using the ECL system (GE
408 Healthcare, Solingen, Germany) for signal detection. Horseradish peroxidase (HRP)-conjugated goat anti
409 rabbit antibody (Roth, Karlsruhe, Germany) served as secondary antibody. Biotin carboxyl carrier protein
410 (BCCP) was detected by horseradish peroxidase-coupled Strep-Tactin (IBA, Göttingen, Germany). The

411 chain formation phenotype was assessed by phase contrast microscopy. SDS sensitivity was determined
412 by aerobic growth in LB medium containing 4% (w/v) sodium dodecyl sulfate (SDS), using the quotient
413 of the OD_{600} with/without SDS after 3 h of growth (Ize et al., 2003). For carbonate washes of membranes,
414 samples were treated as described before (Hou et al., 2018).

415 *Electron microscopy – Sample preparation*: Bacterial cells (20 ml culture, 5 % inoculum) were grown at
416 37°C at 140 rpm to OD_{600} ~0.5, then 0.4 ml of an aqueous 25 mM tetrachloroauric acid solution were
417 added, and growth was continued for 90 min at 37°C and 120 rpm. Cells were sedimented (10 min, 3,820
418 x g, 4°C), resuspended in 1.5 ml 100 mM HEPES pH 7.0, 90 mM sucrose (buffer A) and incubated for
419 5 min at room temperature (RT). Cells were sedimented again (2 min, RT, 6,800 x g) and the
420 incubation/resuspension was repeated. Cells were then resuspended in 1 ml buffer A containing 2.5 %
421 glutaraldehyde, incubated for > 20 min at RT, washed with 1 ml buffer A, sedimented (2 min, 6,177 x g,
422 RT), and washed twice in 100 mM HEPES pH 6.9, 90 mM sucrose, 10 mM $MgCl_2$, 10 mM $CaCl_2$,
423 sedimented again and embedded either in SPURR epoxy resin (Lünsdorf et al., 2001) or in LR-White
424 resin (Fernández de Castro et al., 2017). 70 nm ultrathin sections were cut using an ultramicrotome with
425 a diamond knife (Ultracut; Leica Biosystems, Nussloch, Germany) and picked up with neoprene-coated
426 Cu-grids (300 mesh, hexagonal). *TEM image registration and processing* - Unstained samples were
427 analyzed in the elastic bright-field mode with an in-column energy-filter transmission electron
428 microscope (Libra 120 plus, Zeiss, Oberkochen, Germany). The energy-selecting slit aperture was set to
429 15 eV energy-width, and images were recorded with a cooled bottom-mount 2 x 2 k CCD (SharpEye,
430 Tröndle, Wiesenmoor, Germany) at nominal magnifications from x 12,500 to x 50,000 near Gaussian or
431 at 500 to 1,500 nm underfocus. Data acquisition and spectrum/image-analysis were done using the iTEM
432 software package (Olympus Soft Imaging Solutions Ltd.). Images were further processed with the Corel
433 Draw Graphics Suite X7 (Corel Ltd.). *Parallel Electron Energy-Loss Spectroscopy (PEELS)* - PEELS
434 was done with unstained 35 nm ultrathin sections of epoxy resin-embedded *E. coli* strain DADE/pABS-
435 *tatAB(MT3)*-C with MT3-gold as the only electron dense intracellular material. PEELS registration was
436 performed in the energy range from 30 to 139 eV, specific for the Au-O_{23} edge, with a 100 µm spectrum
437 entrance aperture and 5 acquisition cycles pro record. Spectrum magnification was set to 200-fold, and
438 the illumination aperture to 0.16 mrad with 4 µA emission current; exposure time: 0.2 s, nominal
439 magnification: x 31,500. *Electron spectroscopic element mapping* Data acquisition was performed on
440 well-defined Au-MT3-clusters and the energy-selective slit was set to 8 eV width. Jump-ratio images
441 were registered at 66 eV (= Emax) and 38 eV (= 1st window). These energy-settings were taken from

PEEL spectrum data of the MT3-gold assemblies of interest. Exposure time: 2 s, illumination aperture: 0.63 mrad, nominal magnification: x 31,500.

MD simulation - Molecular dynamics simulations were performed using the GROMACS simulation package, version 2019.5 (Lindahl et al., 2019). The MARTINI v2.1 coarse-grained force field (Marrink et al., 2004; Marrink et al., 2007; Monticelli et al., 2008) was applied to simulate lipids, peptides, and solvent. In all simulations, the system was coupled to a constant temperature bath by v-rescale algorithm (Bussi et al., 2007) with a relaxation time of 1.0 ps. Simulations were performed at 320 K. Periodic boundary conditions were applied to simulate bulk behavior. The time step used in the simulation was 20 fs. The dielectric constant in the simulations was $\varepsilon_r = 15$. The pressure was coupled to 1 bar employing the Parrinello-Rahman barostat (Parrinello & Rahman, 1981) with a relaxation time of 12.0 ps. Unless stated otherwise, the TatA membrane system consisted of 22 TatA proteins in a lipid bilayer with 75 % phosphatidylethanolamine, 19 % phosphatidylglycerol and 6 % cardiolipin, which is a usual ratio of these lipids in the cytoplasmic membrane of *E. coli* (Raetz, 1978). For the MD simulations of TatA associations, a coarse-grained TatA model up to residue Glu47 was constructed based on the known NMR structure (PDB 2MN7, 10). To model the linear assembly of TatA proteins observed in the TEM experiments, 22 copies of the equilibrated TatA structure were placed vis-à-vis in two rows of 11 subunits, and inserted in the membrane via deletion of all overlapping membrane lipids. The overall dimension of these 22-mers, about 20 nm in length, closely match to the ones observed in METTEM. This system was then equilibrated for 500 ns to enable adaption of the membrane. The TMHs readily associated in a staggered way with all TatA proteins included in the linear complex. For all simulations, the TatA sequences up to position Lys49 were used, as C-terminal truncation analyses have shown that a TatA of exactly that length is still functional (Lee et al., 2002). MODELLER 9.24 (Webb & Sali, 2016) was used to create the TatA variants. The resulting data were evaluated by MDAnalysis 0.20.1 (Michaud-Agrawal et al., 2011). The lipid tail order parameter $S_{zz} = \frac{1}{2}(3(\mathbf{b}*\mathbf{n})^2-1)$ was determined to quantify the average orientation of tail bond vectors **b** with respect to the bilayer normal **n** (MacDermaid et al., 2015). Order parameter time series were checked for equilibration and decorrelated using the pymbar package (Chodera et al., 2007; Chodera, 2016; Shirts & Chodera, 2008). Angles between the TMH and the APH were calculated between two vectors connecting the center of masses (COM) of residues Gly21, Thr22, and Lys23 for the hinge either with the COM of residues Ala13, Val14, and Ile15 for the TMH, or with the COM of residues Ile28, Gly29, and Ser30 for the APH (wild type numbering). Images of the simulations were generated using NGLview v2.7.7 (Nguyen et al., 2018).

Acknowledgements

We thank Sybille Traupe and Katrin Gunka (LUH, Hannover) for excellent technical assistance. We gratefully acknowledge the skillful work and experience in electron microscopic sample preparation by Inge Kristen, Sabine Schmidt and Ina Schleicher (HZI, Braunschweig).

Competing interests

The authors declare that no competing interests exist.

Funding

This work was supported by the DFG grant BR2285/8-1.

References

Alcock, F., Baker, M. A. B., Greene, N. P., Palmer, T., Wallace, M. I., & Berks, B. C. (2013). Live cell imaging shows reversible assembly of the TatA component of the twin-arginine protein transport system. *Proceedings of the National Academy of Sciences of the United States of America*, *110*(38), E3650-9. https://doi.org/10.1073/pnas.1306738110

Alcock, F., Stansfeld, P. J., Basit, H., Habersetzer, J., Baker, M. A., Palmer, T., Wallace, M. I., & Berks, B. C. (2016). Assembling the Tat protein translocase. *ELife*, *5*. https://doi.org/10.7554/eLife.20718

Alder, N. N., & Theg, S. M. (2003). Energetics of protein transport across biological membranes. a study of the thylakoid DpH-dependent/cpTat pathway. *Cell*, *112*(2), 231–242. https://doi.org/10.1016/s0092-8674(03)00032-1

Aldridge, C., Ma, X., Gerard, F., & Cline, K. (2014). Substrate-gated docking of pore subunit Tha4 in the TatC cavity initiates Tat translocase assembly. *The Journal of Cell Biology*, *205*(1), 51–65. https://doi.org/10.1083/jcb.201311057

Aldridge, C., Storm, A., Cline, K., & Dabney-Smith, C. (2012). The chloroplast twin arginine transport (Tat) component, Tha4, undergoes conformational changes leading to Tat protein transport. *J Biol Chem*, *287*(41), 34752–34763. https://doi.org/10.1074/jbc.M112.385666

Baeza-Delgado, C., Marti-Renom, M. A., & Mingarro, I. (2013). Structure-based statistical analysis of transmembrane helices. *European Biophysics Journal : EBJ*, *42*(2-3), 199–207. https://doi.org/10.1007/s00249-012-0813-9

Bageshwar, U. K., & Musser, S. M. (2007). Two electrical potential-dependent steps are required for transport by the *Escherichia coli* Tat machinery. *J Cell Biol*, *179*(1), 87–99. https://doi.org/10.1083/jcb.200702082

Behrendt, J., & Brüser, T. (2014). The TatBC complex of the Tat protein translocase in *Escherichia coli* and its transition to the substrate-bound TatABC complex. *Biochemistry*, *53*(14), 2344–2354. https://doi.org/10.1021/bi500169s

Behrendt, J., Lindenstrauss, U., & Brüser, T. (2007). The TatBC complex formation suppresses a modular TatB-multimerization in *Escherichia coli*. *FEBS Letters*, *581*(21), 4085–4090. https://doi.org/10.1016/j.febslet.2007.07.045

Behrendt, J., Standar, K., Lindenstrauss, U., & Brüser, T. (2004). Topological studies on the twin-arginine translocase component TatC. *FEMS Microbiology Letters*, *234*(2), 303–308. https://doi.org/10.1016/j.femsle.2004.03.048

Berks, B. C. (1996). A common export pathway for proteins binding complex redox cofactors? *Mol Microbiol*, *22*(3), 393–404. https://doi.org/10.1046/j.1365-2958.1996.00114.x

Berthelmann, F., & Brüser, T. (2004). Localization of the Tat translocon components in *Escherichia coli*. *FEBS Letters*, *569*(1-3), 82–88. https://doi.org/10.1016/j.febslet.2004.05.054

Bolhuis, A., Mathers, J. E., Thomas, J. D., Barrett, C. M., & Robinson, C. (2001). TatB and TatC form a functional and structural unit of the twin-arginine translocase from *Escherichia coli*. *J Biol Chem*,

276(23), 20213–20219. https://doi.org/10.1074/jbc.M100682200

Bouchet-Marquis, C., Pagratis, M., Kirmse, R., & Hoenger, A. (2012). Metallothionein as a clonable high-density marker for cryo-electron microscopy. *Journal of Structural Biology*, *177*(1), 119–127. https://doi.org/10.1016/j.jsb.2011.10.007

Braun, N. A., Davis, A. W., & Theg, S. M. (2007). The chloroplast Tat pathway utilizes the transmembrane electric potential as an energy source. *Biophys J*, *93*(6), 1993–1998. https://doi.org/10.1529/biophysj.106.098731

Brüser, T., & Sanders, C. (2003). An alternative model of the twin arginine translocation system. *Microbiol Res*, *158*(1), 7–17. https://doi.org/10.1078/0944-5013-00176

Brüser, T., Yano, T., Brune, D. C., & Daldal, F. (2003). Membrane targeting of a folded and cofactor-containing protein. *European Journal of Biochemistry*, *270*(6), 1211–1221. https://doi.org/10.1046/j.1432-1033.2003.03481.x

Bussi, G., Donadio, D., & Parrinello, M. (2007). Canonical sampling through velocity rescaling. *The Journal of Chemical Physics*, *126*(1), 14101. https://doi.org/10.1063/1.2408420

Casadaban, M. J. (1976). Transposition and fusion of the *lac* genes to selected promoters in *Escherichia coli* using bacteriophage lambda and Mu. *J Mol Biol*, *104*(3), 541–555. https://doi.org/10.1016/0022-2836(76)90119-4

Chodera, J. D. (2016). A Simple Method for Automated Equilibration Detection in Molecular Simulations. *Journal of Chemical Theory and Computation*, *12*(4), 1799–1805. https://doi.org/10.1021/acs.jctc.5b00784

Chodera, J. D., Swope, W. C., Pitera, J. W., Seok, C., & Dill, K. A. (2007). Use of the Weighted Histogram Analysis Method for the Analysis of Simulated and Parallel Tempering Simulations. *Journal of Chemical Theory and Computation*, *3*(1), 26–41. https://doi.org/10.1021/ct0502864

Cline, K., & Mori, H. (2001). Thylakoid DpH-dependent precursor proteins bind to a cpTatC-Hcf106 complex before Tha4-dependent transport. *J Cell Biol*, *154*(4), 719–729. https://doi.org/10.1083/jcb.200105149

Cline, K. (2015). Mechanistic Aspects of Folded Protein Transport by the Twin Arginine Translocase (Tat). *J Biol Chem*, *290*(27), 16530–16538. https://doi.org/10.1074/jbc.R114.626820

Dabney-Smith, C., Mori, H., & Cline, K. (2006). Oligomers of Tha4 organize at the thylakoid Tat translocase during protein transport. *J Biol Chem*, *281*(9), 5476–5483. https://doi.org/10.1074/jbc.M512453200

Diestra, E., Fontana, J., Guichard, P., Marco, S., & Risco, C. (2009). Visualization of proteins in intact cells with a clonable tag for electron microscopy. *Journal of Structural Biology*, *165*(3), 157–168. https://doi.org/10.1016/j.jsb.2008.11.009

Fernández de Castro, I., Fernández, J. J., Barajas, D., Nagy, P. D., & Risco, C. (2017). Three-dimensional imaging of the intracellular assembly of a functional viral RNA replicase complex. *Journal of Cell Science*, *130*(1), 260–268. https://doi.org/10.1242/jcs.181586

Fröbel, J., Rose, P., Lausberg, F., Blümmel, A.-S., Freudl, R., & Müller, M. (2012). Transmembrane insertion of twin-arginine signal peptides is driven by TatC and regulated by TatB. *Nature Communications*, *3*, 1311. https://doi.org/10.1038/ncomms2308

Geise, H., Heidrich, E. S., Nikolin, C. S., Mehner-Breitfeld, D., & Brüser, T. (2019). A Potential Late Stage Intermediate of Twin-Arginine Dependent Protein Translocation in *Escherichia coli*. *Frontiers in Microbiology*, *10*. https://doi.org/10.3389/fmicb.2019.01482

Gerard, F., & Cline, K. (2006). Efficient twin arginine translocation (Tat) Pathway transport of a precursor protein covalently anchored to its initial cpTatC binding site. *J Biol Chem*, *281*(10), 6130–6135. https://doi.org/10.1074/jbc.M512733200

Gohlke, U., Pullan, L., McDevitt, C. A., Porcelli, I., Leeuw, E. de, Palmer, T., Saibil, H. R., & Berks, B. C. (2005). The TatA component of the twin-arginine protein transport system forms channel complexes of variable diameter. *Proceedings of the National Academy of Sciences of the United States of America*, *102*(30), 10482–10486. https://doi.org/10.1073/pnas.0503558102

Habersetzer, J., Moore, K., Cherry, J., Buchanan, G., Stansfeld, P. J., & Palmer, T. (2017). Substrate-triggered position switching of TatA and TatB during Tat transport in *Escherichia coli*. *Open*

Biology, *7*(8). https://doi.org/10.1098/rsob.170091

Haldimann, A., & Wanner, B. L. (2001). Conditional-replication, integration, excision, and retrieval plasmid-host systems for gene structure-function studies of bacteria. *Journal of Bacteriology*, *183*(21), 6384–6393. https://doi.org/10.1128/JB.183.21.6384-6393.2001

Holt, A., & Killian, J. A. (2010). Orientation and dynamics of transmembrane peptides: The power of simple models. *European Biophysics Journal : EBJ*, *39*(4), 609–621. https://doi.org/10.1007/s00249-009-0567-1

Hou, B., & Brüser, T. (2011). The Tat-dependent protein translocation pathway. *Biomolecular Concepts*, *2*(6), 507–523. https://doi.org/10.1515/BMC.2011.040

Hou, B., Heidrich, E. S., Mehner-Breitfeld, D., & Brüser, T. (2018). The TatA component of the twin-arginine translocation system locally weakens the cytoplasmic membrane of *Escherichia coli* upon protein substrate binding. *The Journal of Biological Chemistry*, *293*(20), 7592–7605. https://doi.org/10.1074/jbc.RA118.002205

Hu, Y., Zhao, E., Li, H., Xia, B., & Jin, C. (2010). Solution NMR Structure of the TatA Component of the Twin-Arginine Protein Transport System from Gram-Positive Bacterium *Bacillus subtilis*. *J Am Chem Soc.* Advance online publication. https://doi.org/10.1021/ja1053785

Ize, B., Stanley, N. R., Buchanan, G., & Palmer, T. (2003). Role of the *Escherichia coli* Tat pathway in outer membrane integrity. *Mol Microbiol*, *48*(5), 1183–1193. https://doi.org/10.1046/j.1365-2958.2003.03504.x

Jack, R. L., Sargent, F., Berks, B. C., Sawers, G., & Palmer, T. (2001). Constitutive expression of *Escherichia coli tat* genes indicates an important role for the twin-arginine translocase during aerobic and anaerobic growth. *J Bacteriol*, *183*(5), 1801–1804. https://doi.org/10.1128/JB.183.5.1801-1804.2001

Jensen, M. Ø., & Mouritsen, O. G. (2004). Lipids do influence protein function-the hydrophobic matching hypothesis revisited. *Biochimica Et Biophysica Acta*, *1666*(1-2), 205–226. https://doi.org/10.1016/j.bbamem.2004.06.009

Jongbloed, J. D., Grieger, U., Antelmann, H., Hecker, M., Nijland, R., Bron, S., & van Dijl, J. M. (2004). Two minimal Tat translocases in *Bacillus*. *Mol Microbiol*, *54*(5), 1319–1325.

Katsuta, H., Sawada, Y., & Sokabe, M. (2019). Biophysical Mechanisms of Membrane-Thickness-Dependent MscL Gating: An All-Atom Molecular Dynamics Study. *Langmuir : The ACS Journal of Surfaces and Colloids*, *35*(23), 7432–7442. https://doi.org/10.1021/acs.langmuir.8b02074

Laemmli, U. K. (1970). Cleavage of structural proteins during the assembly of the head of bacteriophage T4. *Nature*, *227*(5259), 680–685. https://doi.org/10.1038/227680a0

Leake, M. C., Greene, N. P., Godun, R. M., Granjon, T., Buchanan, G., Chen, S., Berry, R. M., Palmer, T., & Berks, B. C. (2008). Variable stoichiometry of the TatA component of the twin-arginine protein transport system observed by in vivo single-molecule imaging. *Proceedings of the National Academy of Sciences of the United States of America*, *105*(40), 15376–15381. https://doi.org/10.1073/pnas.0806338105

Lee, P. A., Buchanan, G., Stanley, N. R., Berks, B. C., & Palmer, T. (2002). Truncation analysis of TatA and TatB defines the minimal functional units required for protein translocation. *J Bacteriol*, *184*(21), 5871–5879.

GROMACS 2019.5 Source code [Computer software]. (2019). Zenodo.

Lünsdorf, H., Strömpl, C., Osborn, A. M., Bennasar, A., Moore, E. R.B., Abraham, W.-R., & Timmis, K. N. (2001) [26] Approach to analyze interactions of microorganisms, hydrophobic substrates, and soil colloids leading to formation of composite biofilms, and to study initial events in microbiogeological processes. *Methods in Enzymology*, *336*, 317-IN14. https://doi.org/10.1016/s0076-6879(01)36598-9

MacDermaid, C. M., Kashyap, H. K., DeVane, R. H., Shinoda, W., Klauda, J. B., Klein, M. L., & Fiorin, G. (2015). Molecular dynamics simulations of cholesterol-rich membranes using a coarse-grained force field for cyclic alkanes. *The Journal of Chemical Physics*, *143*(24), 243144. https://doi.org/10.1063/1.4937153

Marrink, S. J., Risselada, H. J., Yefimov, S., Tieleman, D. P., & Vries, A. H. de (2007). The MARTINI force

field: Coarse grained model for biomolecular simulations. *The Journal of Physical Chemistry B*, *111*(27), 7812–7824. https://doi.org/10.1021/jp071097f

Marrink, S. J., Vries, A. H. de, & Mark, A. E. (2004). Coarse Grained Model for Semiquantitative Lipid Simulations. *The Journal of Physical Chemistry B*, *108*(2), 750–760. https://doi.org/10.1021/jp036508g

Mercogliano, C. P., & DeRosier, D. J. (2006). Gold nanocluster formation using metallothionein: Mass spectrometry and electron microscopy. *Journal of Molecular Biology*, *355*(2), 211–223. https://doi.org/10.1016/j.jmb.2005.10.026

Mercogliano, C. P., & DeRosier, D. J. (2007). Concatenated metallothionein as a clonable gold label for electron microscopy. *Journal of Structural Biology*, *160*(1), 70–82. https://doi.org/10.1016/j.jsb.2007.06.010

Michaud-Agrawal, N., Denning, E. J., Woolf, T. B., & Beckstein, O. (2011). Mdanalysis: A toolkit for the analysis of molecular dynamics simulations. *Journal of Computational Chemistry*, *32*(10), 2319–2327. https://doi.org/10.1002/jcc.21787

Monticelli, L., Kandasamy, S. K., Periole, X., Larson, R. G., Tieleman, D. P., & Marrink, S.-J. (2008). The MARTINI Coarse-Grained Force Field: Extension to Proteins. *Journal of Chemical Theory and Computation*, *4*(5), 819–834. https://doi.org/10.1021/ct700324x

Mori, H., & Cline, K. (2002). A twin arginine signal peptide and the pH gradient trigger reversible assembly of the thylakoid ΔpH/Tat translocase. *J Cell Biol*, *157*(2), 205–210. https://doi.org/10.1083/jcb.200202048

Morphew, M. K., O'Toole, E. T., Page, C. L., Pagratis, M., Meehl, J., Giddings, T., Gardner, J. M., Ackerson, C., Jaspersen, S. L., Winey, M., Hoenger, A., & McIntosh, J. R. (2015). Metallothionein as a clonable tag for protein localization by electron microscopy of cells. *Journal of Microscopy*, *260*(1), 20–29. https://doi.org/10.1111/jmi.12262

Müller, M., & Klösgen, R. B. (2005). The Tat pathway in bacteria and chloroplasts. *Mol Membr Biol*, *22*(1-2), 113–121. https://doi.org/10.1080/09687860500041809

Nguyen, H., Case, D. A., & Rose, A. S. (2018). Nglview-interactive molecular graphics for Jupyter notebooks. *Bioinformatics (Oxford, England)*, *34*(7), 1241–1242. https://doi.org/10.1093/bioinformatics/btx789

Nishino, Y., Yasunaga, T., & Miyazawa, A. (2007). A genetically encoded metallothionein tag enabling efficient protein detection by electron microscopy. *Journal of Electron Microscopy*, *56*(3), 93–101. https://doi.org/10.1093/jmicro/dfm008

Oates, J., Barrett, C. M. L., Barnett, J. P., Byrne, K. G., Bolhuis, A., & Robinson, C. (2005). The *Escherichia coli* twin-arginine translocation apparatus incorporates a distinct form of TatABC complex, spectrum of modular TatA complexes and minor TatAB complex. *Journal of Molecular Biology*, *346*(1), 295–305. https://doi.org/10.1016/j.jmb.2004.11.047

Pal, D., Fite, K., & Dabney-Smith, C. (2013). Direct interaction between a precursor mature domain and transport component Tha4 during twin arginine transport of chloroplasts. *Plant Physiology*, *161*(2), 990–1001. https://doi.org/10.1104/pp.112.207522

Parrinello, M., & Rahman, A. (1981). Polymorphic transitions in single crystals: A new molecular dynamics method. *Journal of Applied Physics*, *52*(12), 7182–7190. https://doi.org/10.1063/1.328693

Petrů, M., Wideman, J., Moore, K., Alcock, F., Palmer, T., & Doležal, P. (2018). Evolution of mitochondrial TAT translocases illustrates the loss of bacterial protein transport machines in mitochondria. *BMC Biology*, *16*(1), 141. https://doi.org/10.1186/s12915-018-0607-3

Pettersson, P., Patrick, J., Jakob, M., Jacobs, M., Klösgen, R. B., Wennmalm, S., & Mäler, L. (2021). Soluble TatA forms oligomers that interact with membranes: Structure and insertion studies of a versatile protein transporter. *Biochimica Et Biophysica Acta. Biomembranes*, *1863*(2), 183529. https://doi.org/10.1016/j.bbamem.2020.183529

Raetz, C. R. (1978). Enzymology, genetics, and regulation of membrane phospholipid synthesis in *Escherichia coli*. *Microbiological Reviews*, *42*(3), 614–659.

Reimer, L., Zepke, U., Moesch, J., Schulze-Hillert, S., Ross-Messemer, M., Probst, W., & Weimer, E.

(1992). *EELSpectroscopy. A Reference Handbook of Standard Data for Identification and Interpretation of Electron Energy Loss Spectra and for Generation of Electron Spectroscopic Images.* Carl Zeiss, Oberkochen, Germany.

Richter, S., & Brüser, T. (2005). Targeting of unfolded PhoA to the TAT translocon of *Escherichia coli*. *J Biol Chem*, *280*(52), 42723–42730. https://doi.org/10.1074/jbc.M509570200

Rodriguez, F., Rouse, S. L., Tait, C. E., Harmer, J., Riso, A. de, Timmel, C. R., Sansom, M. S., Berks, B. C., & Schnell, J. R. (2013). Structural model for the protein-translocating element of the twin-arginine transport system. *Proceedings of the National Academy of Sciences of the United States of America*, *110*(12), E1092-101. https://doi.org/10.1073/pnas.1219486110

Rollauer, S. E., Tarry, M. J., Graham, J. E., Jaaskelainen, M., Jager, F., Johnson, S., Krehenbrink, M., Liu, S.-M., Lukey, M. J., Marcoux, J., McDowell, M. A., Rodriguez, F., Roversi, P., Stansfeld, P. J., Robinson, C. V., Sansom, M. S. P., Palmer, T., Hogbom, M., Berks, B. C., & Lea, S. M. (2012). Structure of the TatC core of the twin-arginine protein transport system. *Nature*, *492*(7428), 210–214. https://doi.org/10.1038/nature11683

Rose, P., Frobel, J., Graumann, P. L., & Müller, M. (2013). Substrate-dependent assembly of the Tat translocase as observed in live *Escherichia coli* cells. *PloS One*, *8*(8), e69488. https://doi.org/10.1371/journal.pone.0069488

Shirts, M. R., & Chodera, J. D. (2008). Statistically optimal analysis of samples from multiple equilibrium states. *The Journal of Chemical Physics*, *129*(12), 124105. https://doi.org/10.1063/1.2978177

Sievers, F., Wilm, A., Dineen, D., Gibson, T. J., Karplus, K., Li, W., Lopez, R., McWilliam, H., Remmert, M., Söding, J., Thompson, J. D., & Higgins, D. G. (2011). Fast, scalable generation of high-quality protein multiple sequence alignments using Clustal Omega. *Molecular Systems Biology*, *7*, 539. https://doi.org/10.1038/msb.2011.75

Taubert, J., & Brüser, T. (2014). Twin-arginine translocation-arresting protein regions contact TatA and TatB. *Biological Chemistry*, *395*(7-8), 827–836. https://doi.org/10.1515/hsz-2014-0170

Taubert, J., Hou, B., Risselada, H. J., Mehner, D., Lünsdorf, H., Grubmüller, H., & Brüser, T. (2015). Tatbc-independent TatA/Tat substrate interactions contribute to transport efficiency. *PloS One*, *10*(3), e0119761. https://doi.org/10.1371/journal.pone.0119761

Walther, T. H., Grage, S. L., Roth, N., & Ulrich, A. S. (2010). Membrane alignment of the pore-forming component TatA(d) of the twin-arginine translocase from *Bacillus subtilis* resolved by solid-state NMR spectroscopy. *Journal of the American Chemical Society*, *132*(45), 15945–15956. https://doi.org/10.1021/ja106963s

Warren, G., Oates, J., Robinson, C., & Dixon, A. M. (2009). Contributions of the transmembrane domain and a key acidic motif to assembly and function of the TatA complex. *J Mol Biol*, *388*(1), 122–132. https://doi.org/10.1016/j.jmb.2009.02.060

Webb, B., & Sali, A. (2016). Comparative Protein Structure Modeling Using MODELLER. *Current Protocols in Protein Science*, *86*, 2.9.1-2.9.37. https://doi.org/10.1002/cpps.20

Wexler, M., Sargent, F., Jack, R. L., Stanley, N. R., Bogsch, E. G., Robinson, C., Berks, B. C., & Palmer, T. (2000). TatD is a cytoplasmic protein with DNase activity. No requirement for TatD family proteins in sec-independent protein export. *J Biol Chem*, *275*(22), 16717–16722. https://doi.org/10.1074/jbc.M000800200

White, G. F., Schermann, S. M., Bradley, J., Roberts, A., Greene, N. P., Berks, B. C., & Thomson, A. J. (2010). Subunit organization in the TatA complex of the twin arginine protein translocase: A site-directed EPR spin labeling study. *J Biol Chem*, *285*(4), 2294–2301. https://doi.org/10.1074/jbc.M109.065458

Windisch, D., Ziegler, C., Grage, S. L., Bürck, J., Zeitler, M., Gor'kov, P. L., & Ulrich, A. S. (2015). Hydrophobic Mismatch Drives the Interaction of E5 with the Transmembrane Segment of PDGF Receptor. *Biophysical Journal*, *109*(4), 737–749. https://doi.org/10.1016/j.bpj.2015.07.022

Workman, C. T., Yin, Y., Corcoran, D. L., Ideker, T., Stormo, G. D., & Benos, P. V. (2005). Enologos: A versatile web tool for energy normalized sequence logos. *Nucleic Acids Research*, *33*(Web Server issue), W389-92. https://doi.org/10.1093/nar/gki439

Yen, M.-R., Tseng, Y.-H., Nguyen, E. H., Wu, L.-F., & Saier, M. H. (2002). Sequence and phylogenetic

727 analyses of the twin-arginine targeting (Tat) protein export system. *Archives of Microbiology*,
728 *177*(6), 441–450. https://doi.org/10.1007/s00203-002-0408-4

729 Zhang, Y., Hu, Y., Li, H., & Jin, C. (2014). Structural basis for TatA oligomerization: An NMR study of
730 Escherichia coli TatA dimeric structure. *PloS One*, *9*(8), e103157.
731 https://doi.org/10.1371/journal.pone.0103157

732 Zhang, Y., Wang, L., Hu, Y., & Jin, C. (2014). Solution structure of the TatB component of the twin-
733 arginine translocation system. *Biochimica Et Biophysica Acta*, *1838*(7), 1881–1888.
734 https://doi.org/10.1016/j.bbamem.2014.03.015